



Master's thesis
Astrophysical Sciences

Complex refractive index from scattering measurements for acoustically levitated single particles

Mikko Vuori

March 24, 2023

Supervisor(s): Docent Antti Penttilä
Professor Karri Muinonen

Censor(s): Professor Karri Muinonen
Docent, Professor Hannakaisa Lindqvist

UNIVERSITY OF HELSINKI
MASTER'S PROGRAMME IN PARTICLE PHYSICS AND ASTROPHYSICAL SCIENCES

PL 64 (Gustaf Hållströmin katu 2)
FI-00014 University of Helsinki

Acknowledgements

I want to thank my supervisors, Doc. Antti Penttilä and Prof. Karri Muinonen, for enabling me to do my thesis on an interesting research project that evolved throughout the process, as science does. The research for the thesis has sparked my interest in laboratory work and planetary science in general and set a research path for the future, for which I am grateful. Also, a thank you to Doc., Prof. Hannakaisa Lindqvist for being a censor and giving valuable feedback.

A thank you to both of my parents who have supported me through my studies. A huge thank you to all of the new friends I have made during the studies, either through physics or the university in general. Most importantly, to the people who have been on this journey from the very start: Atte, Vesa, Ilari, and Ari. Your overwhelming support, both in studies and personal life, has been vital to my studies. Finally, a thank you to my beloved Elli, who has stuck with me throughout the years.

Tiedekunta — Fakultet — Faculty		Koulutusohjelma — Utbildningsprogram — Education programme	
Faculty of Science		Particle Physics and Astrophysical Sciences	
Tekijä — Författare — Author			
Mikko Vuori			
Työn nimi — Arbetets titel — Title			
Complex refractive index from scattering measurements for acoustically levitated single particles			
Opintosuunta — Studieriktning — Study track			
Astrophysical Sciences			
Työn laji — Arbetets art — Level		Aika — Datum — Month and year	Sivumäärä — Sidoantal — Number of pages
Master's thesis		March 24, 2023	61 pages
Tiivistelmä — Referat — Abstract			
<p>A method for deriving the complex refractive index of a mm-sized single particle in a specific wavelength using laboratory measurements is presented. Laboratory measurements were done using the 4π scatterometer, which measures Mueller matrix elements of a particle suspended in air using acoustic levitation as a function of scattering angle. To obtain the complex refractive index of the particle, measurements were compared to simulations from a newly developed SIRIS4 Fixed Orientation (SIRIS4 FO) geometric optics simulation.</p> <p>The 4π scatterometer is a unique instrument which measures Mueller matrix elements from a particle using linear polarizers and a detector rotating about the particle on a rotational stage. The scatterometer uses an acoustic levitator as a sample holder which provides nondestructive measurements and full orientation control of the sample.</p> <p>To compare the measurement results to simulations, SIRIS4 single-particle geometric optics code was modified to handle particles in a fixed orientation. The original code is able to calculate the Mueller matrix elements for a given 3D model, but averages the results over the orientation of the particle. The modified SIRIS4 FO calculates the Mueller matrix elements over the full solid angle as functions of the two scattering angles, which give the direction of observation of the scattered wave compared to the direction of the incident wave. A 3D model of the shape of the measured particle was constructed using X-ray microtomography, and was translated to SIRIS4 FO.</p> <p>The complex refractive index was obtained with a nonlinear least squares analysis by minimizing the sum of squared residuals between the measurements and simulations with varying refractive index values. Finally, confidence regions were constrained for the results, by estimating the computed residuals between simulations and measurements as the random errors in the nonlinear model.</p>			
Avainsanat — Nyckelord — Keywords			
Light scattering measurements, light scattering simulations, complex refractive index			
Säilytyspaikka — Förvaringsställe — Where deposited			
Muita tietoja — övriga uppgifter — Additional information			

Contents

1	Introduction	1
1.1	Study of light scattering	1
1.2	Complex refractive index	2
1.3	Aims of the thesis	2
2	Light scattering	4
2.1	Electromagnetic wave	4
2.1.1	Scattering matrix	5
2.2	Polarization of light	7
2.2.1	Mueller matrix	8
2.2.2	Vibration ellipse	11
2.3	Complex refractive index	12
2.3.1	Analytical solutions	13
2.3.2	Powder samples	14
2.3.3	Single particles	14
2.3.4	Absorption measurements	15
2.3.5	Mixture of materials	15
2.4	Geometric optics	15
2.4.1	Inhomogeneous waves	18
3	Geometric optics framework SIRIS4	20
3.1	SIRIS4 light scattering code	20
3.1.1	Ray tracing	21
3.1.2	Surface reflection and refraction	22
3.1.3	Diffuse scattering	22
3.2	Gaussian-random-sphere particles	23
3.3	SIRIS4 Fixed Orientation	24
4	4π scatterometer	26

4.1	4π scatterometer setup	27
4.1.1	Light source	28
4.1.2	Sample holder	28
4.1.3	Detector	30
4.1.4	Light source intensity monitor	30
4.1.5	Imaging system	31
4.1.6	Computer interface	31
4.2	Measurement steps	32
4.2.1	Mueller matrix of the sample	33
4.2.2	Data reduction and accuracy of measurements	34
5	Laboratory samples	36
5.1	3D modeling of laboratory samples	37
5.2	Omnidirectional microscopy	39
6	Measurements	41
6.1	Calibration measurements	41
6.2	Random orientation	43
6.3	Fixed orientation	44
7	Results for complex refractive index	47
8	Conclusions	55
	Bibliography	57

1. Introduction

1.1 Study of light scattering

The scattering of light can be described macroscopically using classical electrodynamics which describes the behavior of electromagnetic radiation (Born, 1999). Light scattering is the process of electromagnetic waves encountering an obstruction, and their propagation path being changed in the process (Mayinger and Feldmann, 2001). The collective interactions of these waves can be described by reflection, refraction, diffraction, and absorption phenomena (Bohren and Huffman, 2008). The electromagnetic waves are described by their wavelength, and all scattering phenomena are wavelength-dependent.

How a material interacts with incoming light depends on the complex refractive index of the material. The complex refractive index is given by its real and imaginary parts. The complex refractive index describes how the oscillations of the charges in the matter, caused by the incident electromagnetic wave, change the propagation of the wave itself. (Bohren and Huffman, 2008)

Light scattering from a particle depends on the particle size, shape, and material. To infer light scattering from a particle with known properties is a forward problem. To deduce the particle properties, which define the light scattering, from scattered light is then an inverse problem. There are no unique solutions to the inverse problem of light scattering, and the solutions usually rely on solutions to the forward problem. Experimental and numerical models are needed to understand light scattering behavior, from which the solutions to the inverse problem can be found. (Bohren and Huffman, 2008)

In the context of the Solar System, light scattering research is crucial when studying objects such as the planets, asteroids, and dust; objects which do not themselves emit light. Light coming from the Sun is scattered by these objects, and the scattered light can be measured to study the properties of the object. Solar System objects consist of multiple different materials, are of different shape, and have

differing surface properties, such as possible regolith on the surface. To model the light scattering from these objects requires extensive knowledge of light scattering effects. (Hovenier and Muñoz, 2009)

1.2 Complex refractive index

The size, shape, and material define light scattering from a sample. To constrain one of these properties, the shape for example, the other properties need to be well defined. How the material affects light scattering is confined to the complex refractive index. The knowledge of the complex refractive index of a material is thus important.

The complex refractive index is not a value that could be measured directly. The solutions to the inverse problem of defining the complex refractive index from light scattering are easier for samples with known properties. Analytical solutions to the problem are available for homogeneous samples with known size and shape. Even slight deviations from these requirements usually make the analytical solutions unusable, and numerical methods need to be utilized. (Bohren and Huffman, 2008) To produce numerical methods to derive the refractive index for differing samples is an active field of study. Different methods need to be utilized depending on the sample properties. In the thesis, a numerical method which utilizes laboratory measurements for deriving the complex refractive index of a mm-sized single-particle is introduced. The laboratory measurements are done using a 4π scatterometer that measures the intensity of polarized light scattered from an acoustically levitated sample as a function of scattering angle.

1.3 Aims of the thesis

The aim of the thesis is to develop a method for deriving the complex refractive index from an acoustically levitated sample in fixed orientation. Measurements are done using the 4π scatterometer, which are then compared to light scattering simulations, to deduce the complex refractive index. To first validate the measurements from the 4π scatterometer, measurements of glass particles in random orientation are compared to results from geometric optics light scattering simulation. Afterwards, the simulation is modified to produce light scattering results from particles in fixed orientation. 4π scatterometer measurements from the glass sample are then compared to the modified light scattering simulations from the same particle. The

real and imaginary parts of the complex refractive index of the particle are deduced by iterating the values in simulations and comparing to measurements.

The thesis is divided into 8 chapters. In chapter 2, some background and motivation to light scattering study is briefly given, with theory on light scattering and geometric optics. Chapter 3 describes the geometric optics framework SIRIS4, used for light scattering simulations, and how it was modified to produce the new SIRIS4 Fixed Orientation code. Chapter 4 describes the working principles and measurement steps of the 4π scatterometer. Chapter 5 discusses the samples used in the study, and the process of creating their 3D geometry models. In chapter 6, the measurements using the 4π scatterometer are described in detail and the pipeline of deriving the refractive index is explained. Chapter 7 describes the results from the measurements and simulations, and the derivation of the complex refractive index. Finally in chapter 8, conclusions are given with some remarks on the future work.

2. Light scattering

Light scattering enables the study of objects remotely. From scattering, the physical properties, which correspond to the material of the object, together with the size and shape of an object can be studied. Scattering from an object includes wave reflection, refraction and diffraction phenomena.

A scattering problem is constructed of two elements; the incident radiation, and the scatterer (Frezza et al., 2018). To formulate the scattering properties of an object from the scattered radiation is an inverse problem. The inverse problem does not have a unique solution and requires assumptions of the scatterer, such as constant bulk optical properties or a measured shape. The optical properties of a material are wavelength dependent, and so are the scattering effects.

Three elements are of interest when studying scattered light: the intensity of the scattered radiation, its polarization, and the directional distribution of the scattering. To solve scattering problems, boundary conditions need to be established. They require the continuity of the tangential components of the electric and magnetic fields at the surface of the scatterer (Frezza et al., 2018).

2.1 Electromagnetic wave

The electromagnetic wave is formulated using Maxwell's equations. Maxwell's equations can be written in terms of free charges and currents,

$$\begin{aligned}\nabla \cdot \vec{D} &= \rho_f, \\ \nabla \times \vec{E} &= -\frac{\partial \vec{B}}{\partial t}, \\ \nabla \cdot \vec{B} &= 0, \\ \nabla \times \vec{H} &= \vec{J}_f + \frac{\partial \vec{D}}{\partial t}.\end{aligned}\tag{2.1}$$

\vec{D} is the electric field displacement, \vec{E} and \vec{B} the electric field and magnetic flux density, and \vec{H} the magnetic field. ρ_f is the free-charge density and \vec{J}_f free-current

density. The equations are supplemented by constitutive relations, which give \vec{D} and \vec{H} in terms of \vec{E} and \vec{B}

$$\begin{aligned}\vec{D} &= \epsilon \vec{E}, \\ \vec{H} &= \frac{1}{\mu} \vec{B},\end{aligned}\tag{2.2}$$

where $\epsilon = \epsilon_0(1 + \chi_e)$ and $\mu = \mu_0(1 + \chi_m)$. In a non-magnetic space where there is no charge or current ($\chi_m = 0$, $\chi_e = 0$, $\rho_f = 0$, $\vec{J}_f = 0$), the Maxwell's equations can be written

$$\begin{aligned}\nabla \cdot \vec{E} &= 0, \\ \nabla \times \vec{E} &= -\frac{\partial \vec{B}}{\partial t}, \\ \nabla \cdot \vec{B} &= 0, \\ \nabla \times \vec{B} &= \mu_0 \epsilon_0 \frac{\partial \vec{E}}{\partial t}.\end{aligned}\tag{2.3}$$

The equations couple the electric field \vec{E} and the magnetic field \vec{B} . They can be separated to second-order differential equations in relation to \vec{E} and \vec{B} ,

$$\begin{aligned}\nabla^2 \vec{E} - \mu_0 \epsilon_0 \frac{\partial^2 \vec{E}}{\partial t^2} &= 0, \\ \nabla^2 \vec{B} - \mu_0 \epsilon_0 \frac{\partial^2 \vec{B}}{\partial t^2} &= 0.\end{aligned}\tag{2.4}$$

A plane wave solution can be found for the equations of the form,

$$\begin{aligned}\vec{E} &= \vec{E}_0 \exp(i\vec{k}z - i\omega t), \\ \vec{B} &= \vec{B}_0 \exp(i\vec{k}z - i\omega t).\end{aligned}\tag{2.5}$$

\vec{E}_0 and \vec{B}_0 are constant complex vectors, ω is an angular frequency, and \vec{k} a wave vector. The electromagnetic field is now presented as a wave equation everywhere in space, with respect to time. With appropriate boundary conditions on the surface of the particle studied, and radiation conditions at infinity, unique solutions can be found for the scattering of light, using the wave equations. (Griffiths, 2017)

2.1.1 Scattering matrix

The electric field in Equation (2.5) can be expressed as the fields parallel \parallel and perpendicular components \perp ,

$$\vec{E}_0 = E_{\parallel} \hat{e}_{\parallel} + E_{\perp} \hat{e}_{\perp}.\tag{2.6}$$

E_{\parallel} and E_{\perp} are determined by the amplitude a and phase δ of the wave,

$$\begin{aligned} E_{\parallel} &= a_{\parallel} e^{-i\delta_{\parallel}}, \\ E_{\perp} &= a_{\perp} e^{-i\delta_{\perp}}. \end{aligned} \quad (2.7)$$

Scattering from an arbitrary particle is defined by the incident field \vec{E}_i and the scattered field \vec{E}_s . The scattering event can be described with a scattering plane pictured in Figure 2.1, and the angles associated with it. The incident field, coming from the xy plane, is defined as in Equation (2.5) and (2.6),

$$\vec{E}_i = (E_{0\parallel} \hat{e}_{\parallel i} + E_{0\perp} \hat{e}_{\perp i}) \exp(ikz - i\omega t) = E_{\parallel i} \hat{e}_{\parallel i} + E_{\perp i} \hat{e}_{\perp i}. \quad (2.8)$$

The scattered field is then,

$$\vec{E}_s = E_{\parallel s} \hat{e}_{\parallel s} + E_{\perp s} \hat{e}_{\perp s}. \quad (2.9)$$

Far away from the particle, the scattered field has the form of a transverse spherical

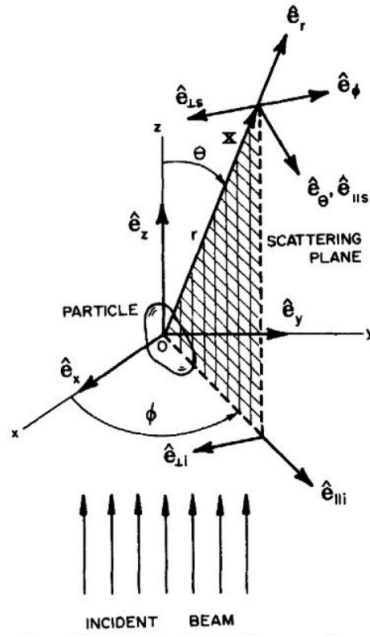


Figure 2.1: The scattering plane and the angles resulting from its geometry are defined by the incident beam and the \vec{x} vector. The incident beam is orthogonal to the xy plane and vector \vec{x} gives the direction of the observer. (Bohren and Huffman, 2008).

wave,

$$\vec{E}_s = \frac{\exp(ikr)}{-ikr} \vec{A}, \quad \hat{e}_r \cdot \vec{A} = 0. \quad (2.10)$$

A relation is now found between the incident and the scattered field. It can be written in matrix form,

$$\begin{pmatrix} E_{\parallel s} \\ E_{\perp s} \end{pmatrix} = \frac{\exp[ik(r-z)]}{-ikr} \begin{pmatrix} S_2 & S_3 \\ S_4 & S_1 \end{pmatrix} \begin{pmatrix} E_{\parallel i} \\ E_{\perp i} \end{pmatrix}. \quad (2.11)$$

The 2×2 matrix is called the amplitude scattering matrix. Its components depend on the scattering angle θ and azimuthal angle ϕ . The scattering equation (2.11) describes a scattered wave with respect to the incident field and the scatterer properties, which are included in the amplitude scattering matrix. (Bohren and Huffman, 2008)

2.2 Polarization of light

Polarization describes the geometric orientation of oscillations in a wave. For light, polarization is usually used to describe the oscillation of the electric field component. Light is called unpolarized if the direction of the electric field fluctuates randomly in time. Scattering events change the polarization of light. The change in polarization is credited to the properties of the scatterer. The scatterer can be thus studied using polarized light. (Hansen and Travis, 1974)

Polarization can be presented as the amplitudes of the perpendicular and parallel components of an electromagnetic wave. Time-averaged polarization properties of a wave can be represented using Stokes parameters, which can be formulated using the parallel and perpendicular components of a wave,

$$\begin{aligned} I &= \langle E_{\parallel} E_{\parallel}^* + E_{\perp} E_{\perp}^* \rangle, \\ Q &= \langle E_{\parallel} E_{\parallel}^* - E_{\perp} E_{\perp}^* \rangle, \\ U &= \langle E_{\parallel} E_{\perp}^* + E_{\perp} E_{\parallel}^* \rangle, \\ V &= \langle i(E_{\parallel} E_{\perp}^* - E_{\perp} E_{\parallel}^*) \rangle. \end{aligned} \quad (2.12)$$

The Stokes parameters $\vec{S} = (I, Q, U, V)$ describe intensities of polarized light, if it would be measured through a polarizer. The components are time averages of the wave components, which means that the Stokes parameters can be used to represent unpolarized or arbitrarily polarized light. I gives the total intensity of both parallel and perpendicular polarizations, Q gives the intensity difference between parallel and perpendicular polarizations, U the difference between $+45^\circ$ and -45° polarizations, and V describes circular polarization by giving the difference between right-handed and left-handed circular polarizations. Visual presentation of the Stokes parameters is given in Figure 2.2. (Hansen and Travis, 1974)

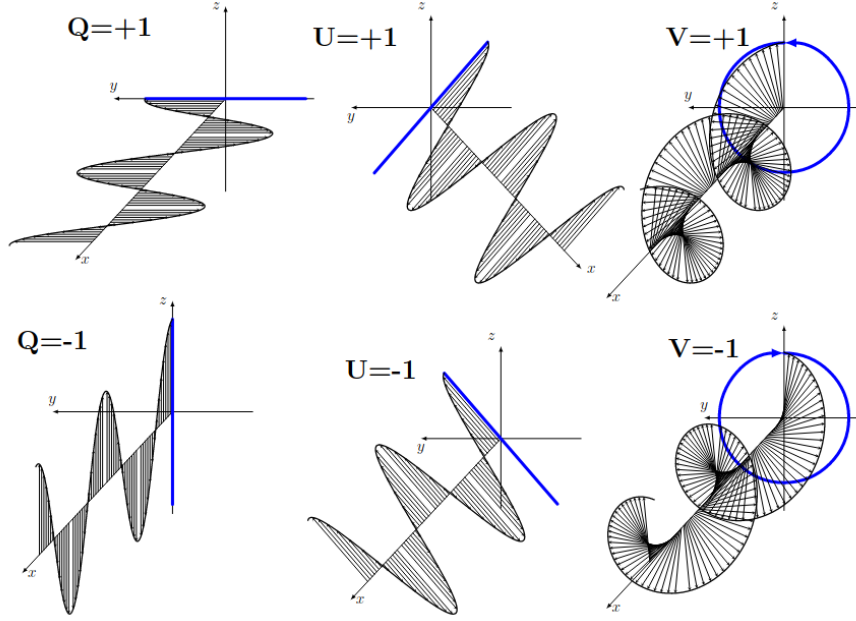


Figure 2.2: The Stokes parameters presented visually, in reference to the propagation plane. The sign of the parameters gives the orientation of the oscillation. The intensity parameter I gives the amplitude of the oscillation, and is not related to the geometry. The circular polarization in V is caused by the two oscillating components traveling in different phases, and the head of the wave drawing a circular pattern as it travels. (Väisänen, 2020)

2.2.1 Mueller matrix

The change of Stokes parameters, as the light encounters a particle, can be expressed from the amplitude scattering matrix in Equation (2.11) using a 4×4 matrix called the Mueller matrix,

$$\begin{pmatrix} I_s \\ Q_s \\ U_s \\ V_s \end{pmatrix} = \frac{1}{k^2 r^2} \begin{pmatrix} S_{11} & S_{12} & S_{13} & S_{14} \\ S_{21} & S_{22} & S_{23} & S_{24} \\ S_{31} & S_{32} & S_{33} & S_{34} \\ S_{41} & S_{42} & S_{43} & S_{44} \end{pmatrix} \begin{pmatrix} I_i \\ Q_i \\ U_i \\ V_i \end{pmatrix}. \quad (2.13)$$

A Mueller matrix describes the change of Stokes parameters in an event that changes polarization. Such an event can be the light transmitting through a polarizer, or light scattering from a particle, as pictured in Figure 2.3. In scattering by a particle, the S_{ij} matrix is commonly known as the scattering matrix. Its elements are given

with the elements of the amplitude scattering matrix, (Bohren and Huffman, 2008)

$$\begin{aligned}
S_{11} &= \frac{1}{2}(|S_1|^2 + |S_2|^2 + |S_3|^2 + |S_4|^2), \\
S_{12} &= \frac{1}{2}(|S_2|^2 - |S_1|^2 + |S_4|^2 - |S_3|^2), \\
S_{13} &= \text{Re}(S_2 S_3^* + S_1 S_4^*), \\
S_{14} &= \text{Im}(S_2 S_3^* - S_1 S_4^*), \\
S_{21} &= \frac{1}{2}(|S_2|^2 - |S_1|^2 - |S_4|^2 + |S_3|^2), \\
S_{22} &= \frac{1}{2}(|S_2|^2 + |S_1|^2 - |S_4|^2 - |S_3|^2), \\
S_{23} &= \text{Re}(S_2 S_3^* - S_1 S_4^*), \\
S_{24} &= \text{Im}(S_2 S_3^* + S_1 S_4^*), \\
S_{31} &= \text{Re}(S_2 S_4^* + S_1 S_3^*), \\
S_{32} &= \text{Re}(S_2 S_4^* - S_1 S_3^*), \\
S_{33} &= \text{Re}(S_1 S_2^* + S_3 S_4^*), \\
S_{34} &= \text{Im}(S_2 S_1^* + S_4 S_3^*), \\
S_{41} &= \text{Im}(S_2^* S_4 + S_3^* S_1), \\
S_{42} &= \text{Im}(S_2^* S_4 - S_3^* S_1), \\
S_{43} &= \text{Im}(S_1 S_2^* - S_3 S_4^*), \\
S_{44} &= \text{Re}(S_1 S_2^* + S_3 S_4^*).
\end{aligned} \tag{2.14}$$

With the scattering matrix, the Stokes parameters of light can be formulated if the amplitude scattering matrix elements can be derived. Vice versa the scattering matrix elements for the scattering particle can be derived by measuring the intensity of differently polarized scattered light. The scattering matrix elements are representative of the material and shape of the particle. The scattering particle can thus be studied by measuring polarization of the scattered field. The amount of independent scattering matrix elements may be reduced due to the scatterer symmetries, or if the scatterer is a collection of randomly orientated particles (Kemppinen et al., 2015).

A general form for the Mueller matrix \mathbf{M} describes any polarizing event,

$$\vec{S}_1 = \mathbf{M} \vec{S}_0. \tag{2.15}$$

The Mueller matrix describes the change in polarization, as arbitrarily polarized light interacts with a polarizing component. These components can be for example polarizing filters. If multiple polarizers would be in line with the incident light, the

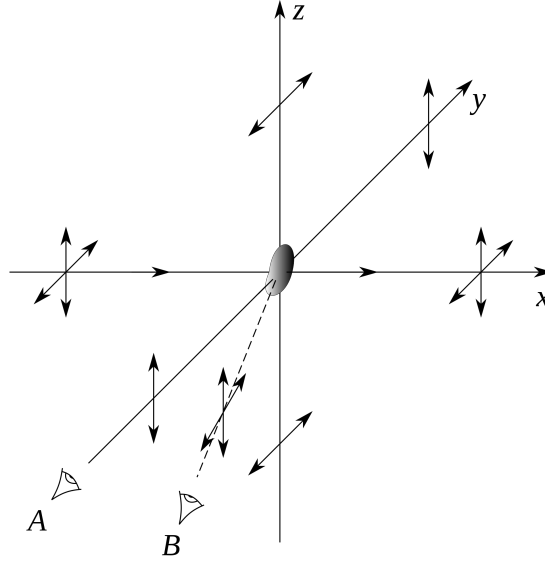


Figure 2.3: Unpolarized light incident on a dust particle changes polarization in the scattering process. The change in polarization varies based on the viewing angle. (Persson, 2013)

effect of all of the components could easily be presented as multiplication of their Mueller matrixes (Hunt and Huffman, 1973).

Polarizers manipulate light, creating a beam with a well-defined polarization. Polarizers are also used when measuring polarization, as specific polarizations can be filtered out, and the resulting intensity measured. The polarizers can simply be presented using a Mueller matrix for the component. For example, an ideal linear polarizer transmits only the electric field components parallel to an axis the wave passes through the polarizer, called the transmission axis. For such a wave, the incident and transmitted components are related through,

$$\begin{pmatrix} E_{\parallel t} \\ E_{\perp t} \end{pmatrix} = \begin{pmatrix} \cos^2 \xi & \sin \xi \cos \xi \\ \sin \xi \cos \xi & \sin^2 \xi \end{pmatrix} \begin{pmatrix} E_{\parallel i} \\ E_{\perp i} \end{pmatrix}, \quad (2.16)$$

where ξ is the angle between \hat{e}_{\parallel} and the transmission axis. The resulting Mueller matrix of the linear polarizer is,

$$\frac{1}{2} \begin{pmatrix} 1 & \cos 2\xi & \sin 2\xi & 0 \\ \cos 2\xi & \cos^2 2\xi & \cos 2\xi \sin 2\xi & 0 \\ \sin 2\xi & \sin 2\xi \cos 2\xi & \sin^2 2\xi & 0 \\ 0 & 0 & 0 & 0 \end{pmatrix}. \quad (2.17)$$

If the transmission axis is orthogonal to the linear polarizer ($\xi = 0^\circ$), the Mueller

matrix simplifies to,

$$\frac{1}{2} \begin{pmatrix} 1 & 1 & 0 & 0 \\ 1 & 1 & 0 & 0 \\ 0 & 0 & 0 & 0 \\ 0 & 0 & 0 & 0 \end{pmatrix}. \quad (2.18)$$

Using the knowledge that the total effect of multiple polarizing components can be found by multiplying their Mueller matrixes, a circular polarizer can be constructed using a linear polarizer and a quarter-wave plate. A quarter-wave plate introduces a phase shift between the parallel and perpendicular components of a wave. The Mueller matrix for a quarter-wave plate, orthogonal to the transmission axis, is given as,

$$\begin{pmatrix} 1 & 0 & 0 & 0 \\ 0 & 0 & 0 & -1 \\ 0 & 0 & 1 & 0 \\ 0 & 1 & 0 & 0 \end{pmatrix}. \quad (2.19)$$

The Mueller matrix for a system containing both of the components is obtained using matrix multiplication

$$\frac{1}{2} \begin{pmatrix} 1 & 1 & 0 & 0 \\ 1 & 1 & 0 & 0 \\ 0 & 0 & 0 & 0 \\ 0 & 0 & 0 & 0 \end{pmatrix} \begin{pmatrix} 1 & 0 & 0 & 0 \\ 0 & 0 & 0 & -1 \\ 0 & 0 & 1 & 0 \\ 0 & 1 & 0 & 0 \end{pmatrix} = \frac{1}{2} \begin{pmatrix} 1 & 1 & 0 & 0 \\ 0 & 0 & 0 & 0 \\ 0 & 0 & 0 & 0 \\ 1 & 1 & 0 & 0 \end{pmatrix}. \quad (2.20)$$

The resulting matrix right-circularly polarizes the light, and from the two different polarizers a circular polarizer is constructed. (Bohren and Huffman, 2008)

2.2.2 Vibration ellipse

Polarization can also be presented using a so-called vibration ellipse, sketched in Figure 2.4. As can be seen from Equation (2.5) and (2.6), the propagating electric field traces out an ellipse with the components E_{\parallel} and E_{\perp} . The resulting ellipse can be expressed with its semi-major axis a , semi-minor axis b , and azimuth angle γ . The ellipticity is then given as b/a . Using the vibration ellipse, the Stokes parameters can be written as,

$$\begin{aligned} I &= c^2, \\ Q &= c^2 \cos 2\eta \cos 2\gamma, \\ U &= c^2 \cos 2\eta \sin 2\gamma, \\ V &= c^2 \sin 2\eta, \end{aligned} \quad (2.21)$$

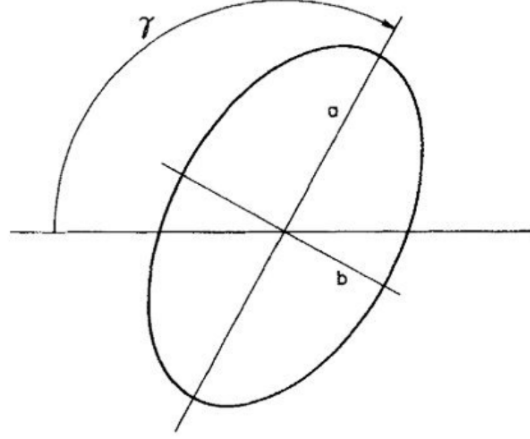


Figure 2.4: Vibration ellipse with semi-major axis a , semi-minor axis b and azimuth angle γ , which gives the angle between the semi-major axis and an arbitrary reference direction (Bohren and Huffman, 2008).

where $c^2 = a^2 + b^2$ and $|\tan \eta| = b/a$. The Mueller matrix can then be used to describe the change of form of the vibration ellipse as the polarization of light changes. (Bohren and Huffman, 2008)

2.3 Complex refractive index

One of the optical properties that fundamentally defines the scattering of light from a particle is the complex refractive index. The refractive index is a complex, wavelength-dependent constant, which describes the refraction and attenuation of light in material. The refractive index is a property of the material, and not dependent on the size and shape of a particle. To know the refractive index of a material is crucial in simulating and understanding a scattering event, for example, to model the scattering of a Solar System body, atmosphere or ocean, as well as biological systems. The refractive index is an important constant in many fields, spanning physics, chemistry, biology, and mineralogy (Bohren and Huffman, 2008).

Maxwell's equations in Equation (2.3) can be written using a plane wave solution for a complex wave vector \vec{k} ,

$$\begin{aligned}\vec{k} \cdot \vec{E} &= 0, \\ \vec{k} \times \vec{E} &= \omega \mu \vec{B}, \\ \vec{k} \cdot \vec{B} &= 0, \\ \vec{k} \times \vec{B} &= -\omega \epsilon \vec{E}.\end{aligned}\tag{2.22}$$

Using the plane wave formalism, the wavenumber $k = |\vec{k}|$ can be defined as

$$k = \omega \sqrt{\epsilon \mu} = \frac{\omega m}{c}, \quad (2.23)$$

where m is now the complex refractive index defined as permeability and permittivity of the medium, in respect to vacuum, (Griffiths, 2017)

$$m = \sqrt{\frac{\epsilon \mu}{\epsilon_0 \mu_0}}. \quad (2.24)$$

The refractive index is defined by its real part n and imaginary part κ :

$$m = n + i\kappa. \quad (2.25)$$

The real part describes the angle of refraction at the boundary of two medium. The imaginary part is commonly called the attenuation coefficient, and it describes the attenuation of light in a medium.

The determination of the refractive index is especially difficult for materials with either very low or high absorption (Bohren and Huffman, 2008). The refractive index in itself is not directly measurable, and needs to be resolved from the inverse scattering problems. Analytical or numerical models need to be compared to scattering measurements. Samples for which the simpler methods of determining the refractive index are valid are homogeneous materials with known size and shape. These kinds of samples include single crystals, slabs of amorphous solids, such as glass, and liquid filled cuvettes (Bohren and Huffman, 2008). Samples returned from space are often found in single particles, and for the valuable specimens the alteration of the sample is not ideal. Unique samples usually require complex models and multiple measurements to deduce the refractive index.

2.3.1 Analytical solutions

To measure the complex refractive index, both the real and imaginary parts need to be solved. This usually requires two different measurements to deduce the two quantities. Analytical solutions to the inverse problem are found by interposing suitable theories to measurements of reflectance, transmittance, and angles of refraction. For materials of high opacity, the real part is measurable from the refraction angle of light using Snel's law. Intensity measurements can be utilized by measuring the reflection and transmission of an homogeneous slab at near-normal incidence. These measurements require a sample opaque enough that transmission measurements are feasible. Reflectance measurements at near-normal incidence can also be done over

a wide wavelength range. Kramers-Kronig analysis can then be utilized to obtain the phase shift of the measured light and deduce the refractive index. Again this method requires an opaque sample, and the measurements need to be extrapolated to apply the Kramers-Kronig analysis. Ellipsometric techniques directly measure the amplitude ratio and phase shift of the reflected light, eliminating the need for Kramers-Kronig analysis and extrapolation. These measurements still require thin opaque slabs and multiple optical elements, making the measurements over a large wavelength range laborious. Measurements using polarized light enable the use of Fresnel formulas. Reflectance can be measured at different polarization states and different incident angles to deduce the refractive index. (Bohren and Huffman, 2008)

2.3.2 Powder samples

The refractive index for particulate samples can be derived from measurements of single particles in the powder, or for the collection of particles. Multiple scattering models can be utilized for a powder if its packing density and the approximate shape and size of the particles are known. For example in Martikainen et al. (2018) the imaginary part of the refractive index was inferred by modeling measured reflectance spectra using ray-tracing codes. Other option is to try to press the loose powder into solid pellets, for which reflection measurements can be utilized. The surface of such pellet can also be polished to make the measurements more exact. The refractive indices derived from the crushed pellets are approximations. The creation of pellets mixes possible orientations of particles in the original material, and overall has a lower reflectance than for example a single crystal would (Long et al., 1993). Both the real and imaginary parts can be inferred from bidirectional reflectance measurements by utilizing for example the Hapke model (Hapke, 2012). Through the Hapke model, the reflectance measurements of powders are related to the single scattering albedo, and the single scattering albedo to the refractive index, if the grain size of the powder is known (Lucey, 1998).

2.3.3 Single particles

Single particles can be studied by comparing scattering measurements to scattering models. In these methods the measured scattering is compared to numerical models of the scattering process, and the refractive index deduced from them. Examples of scattering models used for single particles include the Mie model, which is defined for spherical particles, and the geometric optics approximation, which is used in this

study. (Bohren and Huffman, 2008)

2.3.4 Absorption measurements

The imaginary part of the refractive index describes the attenuation of light in a medium, and can thus be derived from measurements of absorption. This is common practice for example in atmospheric models. Indirect methods to derive the absorption of a sample include diffuse reflection, photoacoustic effect and integrating plates. (Bohren and Huffman, 2008)

2.3.5 Mixture of materials

For a mixture of materials, such as minerals found on Solar System bodies, the definition of refractive index is not unambiguous. For example, the refractive index of an asteroid, or for a mixture of minerals found on the Moon, is calculable, but inferring the refractive index of a single component is complicated. The refractive indices in a mixture are not additive. The refractive index derived using one method, for example by absorption, from a mixture might not be directly applicable to describe reflectance measurements (Bohren and Huffman, 2008).

2.4 Geometric optics

Geometric optics describes light propagation and scattering when the incident plane wave is subdivided into rays. When the local curvature radii are much larger than the wavelength, the incident light can be approximated so that it does not travel as a wave, and can be treated as a ray. (Molesini, 2005) As a result of the ray approximation, geometric optics is valid for particles much larger than the wavelength. Ray tracing is useful when the path of rays traveling inside the particle is of interest. (Winston, 2005) The reflections inside the particle boosts some scattering directions over the others. This causes the scattering phase function to have a distinct shape when the particle is illuminated from a certain direction. Rainbow and halo phenomena are well modeled using geometric optics.

Traditional geometric optics is an approximation which assumes homogeneous plane waves and absorption in the direction of propagation. The propagation of rays at boundaries is governed by Snel's law and Fresnel equations (Bohren and Huffman, 2008). The rays are split in two at boundaries, with one part being reflected and another transmitted. Example of an incident ray reflecting and refracting in the

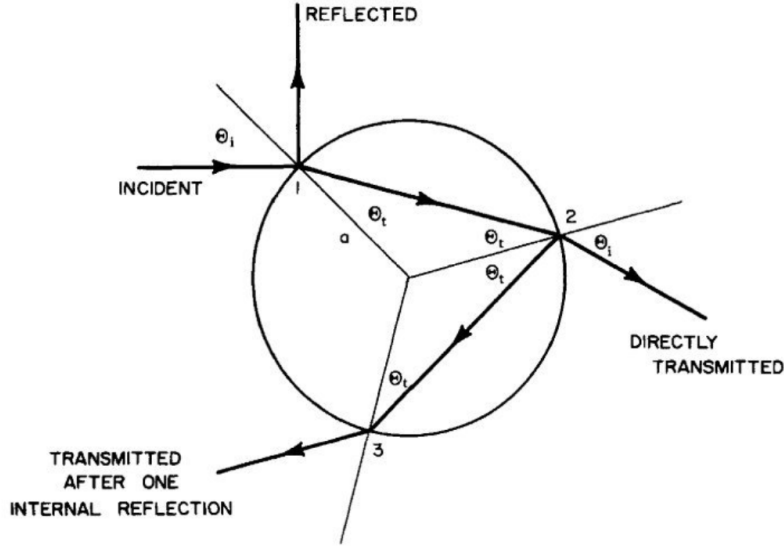


Figure 2.5: Incident ray is split into the reflected and transmitted parts, at a boundary. The angle of refraction is given by Snel's law, and the amplitude of the reflected and refracted rays by the Fresnel equation. (Bohren and Huffman, 2008)

geometric optics approximation on a spherical particle is given in Figure 2.5. Fresnel equations govern the amount of light being reflected and transmitted at a boundary. They are given as amplitude ratios compared to the incident light for the reflected (r) and transmitted (t) light and for parallel and perpendicular polarizations,

$$\begin{aligned}
 r_{\perp} &= \frac{n_1 \cos \theta_i - n_2 \cos \theta_t}{n_1 \cos \theta_i + n_2 \cos \theta_t}, \\
 t_{\perp} &= \frac{2n_1 \cos \theta_i}{n_1 \cos \theta_i + n_2 \cos \theta_t}, \\
 r_{\parallel} &= \frac{n_2 \cos \theta_i - n_1 \cos \theta_t}{n_2 \cos \theta_i + n_1 \cos \theta_t}, \\
 t_{\parallel} &= \frac{2n_1 \cos \theta_i}{n_2 \cos \theta_i + n_1 \cos \theta_t}.
 \end{aligned} \tag{2.26}$$

In the above equations, θ_i is the angle of incidence, θ_t the angle of refraction, n_1 the real part of the refractive index of the surrounding medium, and n_2 that of the particle. The angles at which the rays are refracted θ_t and reflected θ_r can be found using Snel's law and the law of reflection (Born, 1999)

$$\begin{aligned}
 \frac{\sin \theta_i}{\sin \theta_t} &= \frac{n_2}{n_1}, \\
 \theta_r &= \theta_i.
 \end{aligned} \tag{2.27}$$

The rays can also be absorbed. Absorption is considered along the ray path inside and outside the particle. Absorption can be approximated from Beer-Lambert

law, where the intensity I of the light attenuates in distance r exponentially according to an absorption coefficient α ,

$$I = I_0 e^{-\alpha r}. \quad (2.28)$$

The absorption coefficient is defined by the wavelength of the light λ and the imaginary part of the refractive index of the medium κ , (Fox, 2010)

$$\alpha = \frac{4\pi\kappa}{\lambda}. \quad (2.29)$$

Cross sections describe the scattered power in relation to the incident field (Frezza et al., 2018). The absorption cross section σ_{abs} and scattering cross section σ_{sca} can be derived for the particle in the geometric optics approximation. The cross sections describe the total absorbed and scattered power. The total energy absorbed W_{abs} by the particle can be calculated from the energy deposited by the internal rays arising from an incident ray, and then integrating over all incident rays. The fraction of total energy absorbed divided with the total energy of the incident rays gives the absorption cross section,

$$\sigma_{\text{abs}} = \frac{W_{\text{abs}}}{I_i}. \quad (2.30)$$

For weakly absorbing particles, the absorption cross section is roughly proportional to the volume of the particle. As the opacity and size of the particles increases, large part of the absorption takes place near the surface of the particle, and the absorption cross section becomes proportional to the area of the particle instead. (Bohren and Huffman, 2008)

The total energy scattered is the sum of the reflected and transmitted energies $W_{\text{sca}} = W_{\text{refl}} + W_{\text{tr}}$, and the scattering cross section is,

$$\sigma_{\text{sca}} = \frac{W_{\text{sca}}}{I_i}. \quad (2.31)$$

The extinction cross section is the sum of scattering and absorption cross sections, (Bohren and Huffman, 2008)

$$\sigma_{\text{ext}} = \sigma_{\text{sca}} + \sigma_{\text{abs}}. \quad (2.32)$$

The ratio of absorption and scattering can be characterized by the single-scattering albedo ϖ ,

$$\varpi = \frac{\sigma_{\text{sca}}}{\sigma_{\text{ext}}}. \quad (2.33)$$

The cross sections characterize a scatterer and enable the comparison of scattering behaviors of different scatterers (Frezza et al., 2018).

2.4.1 Inhomogeneous waves

In an absorbing media the plane waves need to be treated as inhomogeneous. For inhomogeneous waves, the plane wave in Equation (2.5) takes on a form,

$$\vec{E} = \vec{E}_0 \exp(i\vec{k}z - i\omega t) = \vec{E}_0 \exp(-k_0 K \hat{f} \cdot \vec{r}) \exp(ik_0 N \hat{e} \cdot \vec{r} - i\omega t), \quad (2.34)$$

where \vec{k} is given as the complex wave vector $\vec{k} = k_0(N\hat{e} + iK\hat{f})$, N and K are the apparent refractive index components, \hat{e} and \hat{f} the directions of the propagating wave, and $k_0 = \omega/c$. The above traditional geometric optics approximation is based on the assumption that the imaginary part is small $K\hat{f} \approx 0$, and \hat{e} and \hat{f} are parallel. Snel's law can be given for inhomogeneous waves as functions of the angles θ and ψ , which are the angles of \hat{e} and \hat{f} in respect to the normal of the surface,

$$N_1 \sin \theta_i = N_2 \sin \theta_t, \quad K_1 \sin \psi_i = K_2 \sin \psi_t. \quad (2.35)$$

Using the same formalism, the Fresnel equations can be given as,

$$\begin{aligned} r_{\perp} &= \frac{k_i - k_t}{k_i + k_t}, \\ t_{\perp} &= \frac{2k_i}{k_i + k_t}, \\ r_{\parallel} &= \frac{m_2^2 k_i - m_1^2 k_t}{m_2^2 k_i + m_1^2 k_t}, \\ t_{\parallel} &= \frac{2m_1 m_2 k_i}{m_2^2 k_i + m_1^2 k_t}, \end{aligned} \quad (2.36)$$

where m_1 and m_2 are the complex refractive index of the two media, and $k_i = (N_1 \cos \theta_i + iK_1 \cos \psi_i)$ and $k_t = (N_2 \cos \theta_t + iK_2 \cos \psi_t)$. (Chang et al., 2005) The rays also exponentially attenuate along the ray path l . In the direction of propagation \hat{e} , the wave is attenuated by,

$$\exp(-Kl \cos \alpha), \quad (2.37)$$

where α is the angle between the vectors \hat{e} and \hat{f} ($\cos \alpha = \hat{e} \cdot \hat{f}$). (Lindqvist et al., 2018)

Polarization can be taken into account in the geometric optics approximation. A Stokes vector can be given for every ray, and its values changed according to a Mueller matrix at every reflection and refraction process. The scattered Stokes vector in geometric optics approximation is given as,

$$\vec{S}_s = \frac{\sigma_{\text{sca}}}{4\pi^2} \mathbf{P} \vec{S}_i, \quad (2.38)$$

where now \mathbf{P} is normalized according to its element P_{11} , also called the scattering phase function,

$$\int_{4\pi} P_{11} d\Omega = 4\pi. \quad (2.39)$$

Geometric optics can be extended with a model for diffraction, and how the rays interfere with one another. The diffraction has to be taken into account in the scattering cross section, and is now the sum of the geometric optics cross section combined with the cross section from forward diffraction,

$$\sigma_{\text{sca}} = \sigma_{\text{sca}}^G + \sigma_{\text{sca}}^D. \quad (2.40)$$

Diffraction also affects the scattering matrix. The final scattering matrix is the sum of the geometric optics scattering matrix \mathbf{P}^G in Equation (2.38) and a scattering matrix derived from a diffraction model \mathbf{P}^D , (Lindqvist et al., 2018)

$$\mathbf{P} = \frac{1}{\sigma_{\text{sca}}} (\sigma_{\text{sca}}^G \mathbf{P}^G + \sigma_{\text{sca}}^D \mathbf{P}^D). \quad (2.41)$$

3. Geometric optics framework

SIRIS4

SIRIS4 geometric optics with diffuse scatterers framework is a collection of three adaptations of ray-tracing codes and a Gaussian-random-sphere particle generator. The ray-tracing codes calculate ray-optics with diffuse scatterers. The computations can be done for generated Gaussian-random-sphere particles, or for a given 3D model. In both of the cases the surface of the model is presented as a triangulated 3D mesh. The three different variations of the code are for single particles, single two-layer particles, and multiple particles. The single-particle code is used for homogeneous particles. The two-layer code creates a core-mantle structure for the particle. The multiple-particle code can handle models with multiple different 3D meshes separated from each other, basically a collection of particles. The single-particle implementation was used in the study. The basic principles of the SIRIS4 single-particle code are detailed in this chapter, and the extensive description of the framework can be found in Muinonen et al. (2009); Lindqvist et al. (2018); Martikainen et al. (2018); Väisänen et al. (2020).

3.1 SIRIS4 light scattering code

SIRIS4 deals with inhomogeneous waves in absorbing media. It produces scattering matrix and efficiencies for a particle or, in the case of Gaussian-random-sphere particles, averages for a sample of particles. Instead of updating the Stokes vector of a light ray, a Mueller matrix is related to every ray and its values updated. A ray then holds the information of the combined effect of light scattering processes in the particle, and not the polarization state of the light. At a boundary, the ray is refracted and reflected according to Snel's law and Fresnel's reflection and refraction coefficients. In the radiative transfer part, extinction mean free path length describes the propagation in the medium, and the scattering is described by

the single-scattering albedo and the scattering phase matrix. For the diffraction part, the forward diffraction is calculated using the Kirchhoff approximation.

3.1.1 Ray tracing

A Mueller matrix, as described in Section 2.2.1, is related to a ray. The Mueller matrix handles the polarization in the process. A normalized scattering phase matrix relates the incident to the scattered ray. The ray-optics approximation is defined so that the extinction and absorption cross sections are defined by the ensemble-averaged cross-sectional area of the scattering particle $\langle A \rangle$,

$$\begin{aligned}\sigma_{\text{sca}}^D &= \langle A \rangle, \\ \sigma_{\text{ext}} &= 2\langle A \rangle.\end{aligned}\tag{3.1}$$

The calculated absorption cross section comes from the ray tracing. The single scattering albedo ϖ and asymmetry parameter g , defined by ray tracing are

$$\begin{aligned}\varpi &= \frac{\sigma_{\text{sca}}^{RT}}{\langle A \rangle}, \\ g &= \int_{4\pi} \frac{d\Omega}{4\pi} \cos \theta P_{11},\end{aligned}\tag{3.2}$$

where θ is the scattering angle. The same way as in Equation (2.40), the asymmetry parameter is the sum of the geometric optics g^G and the forward diffraction g^D parts. (Muinonen et al., 2009)

The geometric optics part of the phase matrix comes from the traced rays that have gone through a number of reflection and refraction processes and escaped from the particle to an imaginary detector. The final geometric optics part of the phase matrix and the cross sections are ensemble-averaged over a parameter $\{\mathbf{Q}\}$, which describes the physical properties of the particle,

$$\begin{aligned}\sigma_{\text{sca}}^{RT} &= \langle \sigma_{\text{sca}}^{RT}(\{\mathbf{Q}\}) \rangle, \\ \sigma_{\text{abs}}^{RT} &= \langle \sigma_{\text{abs}}^{RT}(\{\mathbf{Q}\}) \rangle, \\ \mathbf{P}^{RT} &= \frac{1}{\sigma_{\text{sca}}^{RT}} \langle \sigma_{\text{sca}}^{RT}(\{\mathbf{Q}\}) \mathbf{P}^{RT}(\{\mathbf{Q}\}) \rangle.\end{aligned}\tag{3.3}$$

In the forward diffraction part, the phase matrix is described by the silhouette of the particle, given in parameter $r(\phi')$,

$$\begin{aligned}\mathbf{P}^D &\propto \frac{k}{4\pi\langle A \rangle} \langle |u(\theta, \phi)|^2 \rangle (1 + \cos \theta)^2 \mathbf{1}, \\ u(\theta, \phi) &= \int_0^{2\pi} d\phi' \int_0^{r(\phi')} dr' r' \exp[-ikr' \sin \theta \cos(\phi - \phi')],\end{aligned}\tag{3.4}$$

where $\mathbf{1}$ is 4×4 unit matrix. The diffraction part of the phase matrix is also normalized as in Equation (2.39). (Muinonen et al., 2009)

3.1.2 Surface reflection and refraction

At the boundary of medium and particle, the reflection and refraction is depicted by Snel's law (2.35) and Fresnel's coefficients (2.36). The Mueller matrices of reflected (\mathbf{M}_R) and refracted (\mathbf{M}_T) rays are given by the Mueller matrices of reflection \mathbf{R} and refraction \mathbf{T} ,

$$\begin{aligned}\mathbf{M}_R &= \mathbf{R} \cdot \mathbf{K} \cdot \mathbf{M}_{\text{inc}}, \\ \mathbf{M}_T &= \mathbf{T} \cdot \mathbf{K} \cdot \mathbf{M}_{\text{inc}},\end{aligned}\tag{3.5}$$

where \mathbf{K} is a rotation matrix, giving the rotation from the ray to the plane of incidence. The rays also exponentially attenuate according to Equation (2.37). (Muinonen et al., 1996)

3.1.3 Diffuse scattering

Inside the particle, SIRIS4 calculates diffuse and specular interactions from internal diffuse scatterers. Inside the particle the diffuse scattering is given by the single-scattering albedo ϖ_0 , extinction mean free path length l_0 , and a scattering phase matrix \mathbf{P}_0 . This internal medium consists of diffuse scatterers embedded in a homogeneous and isotropic medium described by the refractive index m . The scattering phase matrix of the inhomogenities can be defined by the user, or an empirical double Henyey-Greenstein (2HG) matrix can be generated from the Rayleigh scattering phase matrix. The 2HG matrix is defined with four parameters: the asymmetry parameter g_0 , the forward and backward symmetries g_1 and g_2 , and the maximum polarization parameter P_0 . The scattering matrix, using the 2HG single-scattering phase function $P_{2\text{HG}}$, is of the form

$$\begin{aligned}\mathbf{P}_0 &= \frac{P_{2\text{HG}}(\theta)}{\frac{1}{2}(1 + \cos^2 \theta)} \begin{pmatrix} \frac{1}{2}(1 + \cos^2 \theta) & -\frac{1}{2}P_0 \sin^2 \theta & 0 & 0 \\ -\frac{1}{2}P_0 \sin^2 \theta & \frac{1}{2}(1 + \cos^2 \theta) & 0 & 0 \\ 0 & 0 & \cos \theta & 0 \\ 0 & 0 & 0 & \cos \theta \end{pmatrix}, \\ P_{2\text{HG}}(\theta) &= w_0 \frac{1 - g_1^2}{(1 + g_1^2 - 2g_1^2 \cos \theta)^{3/2}} + (1 - w_0) \frac{1 - g_2^2}{(1 + g_2^2 - 2g_2^2 \cos \theta)^{3/2}}, \\ g_0 &= w_0 g_1 + (1 - w_0) g_2,\end{aligned}\tag{3.6}$$

where w_0 is the normalized weight of the first Henye-Greenstein function obtained from the symmetries $w_0 = \frac{g_0 - g_2}{g_1 - g_2}$. At each scattering event, the new scattering angle θ is generated from the P_{11} element. (Muinonen et al., 2009)

3.2 Gaussian-random-sphere particles

A Gaussian-random-sphere particle is analogous to an infinite ensemble of particles drawn from a probability density function for the Gaussian random sphere. In practice an ensemble of particles can be represented using a Gaussian particle, if the underlying distribution for the ensemble is known. A Gaussian sphere is described in spherical coordinates (ϑ, φ) by the spherical-harmonics series for the logarithmic radial distance s :

$$\begin{aligned} r(\vartheta, \varphi) \mathbf{e}_r &= \frac{a \exp[s(\vartheta, \varphi)]}{\sqrt{1 + \sigma^2}} \mathbf{e}_r, \\ s(\vartheta, \varphi) &= \sum_{l=0}^{\infty} \sum_{m=-l}^l s_{lm} Y_{lm}(\vartheta, \varphi), \end{aligned} \tag{3.7}$$

where a is the mean and σ the relative standard deviation of radial distance, s_{lm} the Gaussian random variables, and Y_{lm} orthonormal spherical harmonics. The auto-covariance of two random variables $s(\vartheta_1, \varphi_1)$ and $s(\vartheta_2, \varphi_2)$, an angular distance γ apart, is described with Σ_s and is defined with a series of Legendre polynomials P_l and coefficient C_l :

$$\begin{aligned} \Sigma_s(\gamma) &= \sum_{l=0}^{\infty} C_l P_l(\cos \gamma), \\ \sum_{l=0}^{\infty} C_l &= \ln(1 + \sigma^2). \end{aligned} \tag{3.8}$$

The Gaussian random sphere is now defined with a , σ and C_l . The coefficient C_l can further be parameterized (correlation lengths $l < 2$ do not correspond to real angles)

$$\begin{aligned} C_0 &= C_1 = 0, \\ C_l &= \frac{\tilde{C}}{l^\nu}, \\ \tilde{C} &= \ln(1 + \sigma^2) \left(\sum_{l=0}^{\infty} \frac{1}{l^\nu} \right)^{-1}. \end{aligned} \tag{3.9}$$

The variable \tilde{C} is a normalization constant, which is parameterized by the standard deviation σ and a power-law index ν . The Gaussian sphere can be described using

the two parameters; standard deviation σ and power-law index ν . (Muinonen et al., 1996, 2009)

3.3 SIRIS4 Fixed Orientation

In their original state, the SIRIS4 ray-tracing codes calculate scattering from an object in random orientation, as a function of one of the spherical coordinates θ while averaging the scattering over the ϕ angle. The particle is also rotated to a random orientation every time a new ray is generated. This is beneficial when an average from an ensemble of particles is of interest, for example, in the case of aerosols. In its core, the ray-tracing method traces the ray path using both of the spherical angles. As the orientation averaging is removed, a simulation is produced from the scattering of light from a particle to the full solid angle.

Each ray that escapes from the particle needs to be gathered to an imaginary detector, which is defined with solid angles of constant intervals. This is already implemented in the original SIRIS4 as scattering angle bins corresponding to the θ angle. When averaging over the whole ϕ angle, the area of the bin which contribute to the chance of rays hitting it, is defined only by the θ angle. The bins are finally normalized to exclude the effect of the bin size from the Monte Carlo simulation. In the modified version of SIRIS4, capable of handling fixed orientation, the ϕ -angle step size has to be taken into account in the size of the bin and in the final normalization of the results. This modified version is called SIRIS4 Fixed Orientation (SIRIS4 FO).

The random orientation was changed to handle a user-defined orientation of the particle. The original orientation of the particle is given in the 3D model of the sample. SIRIS4 FO also has an orientation control that can rotate the particle using the Euler angles (α, β, γ) , which give the orientation of a body with respect to a fixed coordinate system.

The amount of rays needed with the SIRIS4 FO to obtain the same accuracy as with the random orientation is the amount of ϕ bins times the amount of rays with the original SIRIS4 single-particle. This directly correlates to the run time of the code, meaning that even with only 10 ϕ -bins being 36° apart, the run time is 10 times larger. To obtain accurate simulations of the small surface texture of the sample requires hundreds of times more rays to that of the random orientation.

To validate the newly modified code, scattering measurements from orientationally controlled glass samples were compared to the simulation results. The

detailed description of validation measurements is given in Section 6.3.

4. 4π scatterometer

One of the first scatterometers was built by Hunt and Huffman (1973). The main goal of a scatterometer is to measure the scattering matrix elements as a function of scattering angle. The scattering matrix was earlier measured successfully using intensity measurements from a scatterer with multiple different polarizing and wavelength filters mounted after the light source and before the receiver (Holland and Gagne, 1970). The innovation by Hunt and Huffman (1973) was the use of polarization modulators to achieve different polarization states. The use of the modulators eliminated inaccuracies in earlier measurements. They measured small polystyrene latex spheres dispersed in water in a cylindrical container, which produce Rayleigh-type scattering in optical wavelengths. As a light source the scatterometer used a high-pressure Hg lamp and could measure angles between 5° and 168° . The results were compared against results from Mie theory.

Based on the scatterometer by Hunt and Huffman (1973), a new model was built by Kuik et al. (1991). This scatterometer was built to measure the scattering matrix of an ensemble of small particles. As a light source it used a He-Ne laser, which produced linearly polarized light with 632.8 nm wavelength. The measurement angle ranged from 5° to 175° . The main differences compared to the earlier scatterometer was the use of a jet of particles instead of a container, which can produce unwanted polarizing effects. The new scatterometer was also able to derive all the scattering matrix elements during one measurement sweep. The Kuik et al. (1991) scatterometer also used three detectors evenly mounted on the rotating pedestal. The use of multiple detectors reduces the measurement time. Shorter measurement time improves the accuracy of the measurements by reducing variations in the sample, such as the stability of the jet. Using the setup, they measured irregularly shaped quartz (SiO_2) particles. The validity of the measurements was analyzed by comparing to Mie theory.

A scatterometer, similar to those by Hunt and Huffman (1973) and Kuik et al. (1991), was built to directly measure the scattering matrix of different aerosol sam-

ples (Volten et al., 2001). The scatterometer has a measurement angle from 5° to 173° , and uses a jet stream of particles produced by an aerosol generator. Two interchangeable lasers were used as a light source; He-Ne (632.8 nm) and He-Cd (441.6 nm). To validate the setup, they measured 7 different aerosol samples; feldspar, red clay, quartz, loess, two kinds of volcanic ash, and Sahara sand. The measured aerosols had different sizes ranging from $0.1\text{ }\mu\text{m}$ to $100\text{ }\mu\text{m}$. The measurements were compared to a ray-optics approximation by Muinonen et al. (1996), which is able to model complex aerosol shapes by modeling the particles as Gaussian spheres. This code was a precursor to SIRIS4.

The scatterometer by Volten et al. (2001) was further improved by Muñoz et al. (2010). They used a similar setup, but with the measurement angles extended to 3° – 177° . The improved setup uses a tunable argon-krypton laser that emits wavelengths of 483, 488, 520, 568, and 647 nm.

This is not an exhaustive list of all scatterometers in the world, but a preview of previous work. Our scatterometer setup, called the 4π scatterometer, is a continuation of this development process, and is similar to the system by Muñoz et al. (2010). Before the 4π scatterometer, there was no system to measure the scattering matrix of a fixed particle of μm to mm size. Our scatterometer is built with controlled orientation in mind, and its main characteristic is the ultrasonic levitator sample holder, with which total control of the sample is achieved. (Recently, a scatterometer using ultrasonic levitation to measure liquid droplets has been built by Onofri et al. (2015).) The light source in our setup uses white light source, which is filtered to needed wavelengths. The process of building the 4π scatterometer and its earlier versions are detailed in Maconi et al. (2017); Penttilä et al. (2017); Maconi et al. (2018); Kassamakov et al. (2018); Muinonen et al. (2019); Maconi et al. (2020). The 4π scatterometer in its current state is extensively described in the following chapter.

4.1 4π scatterometer setup

The 4π scatterometer is composed of components in five groups: light source, sample holder, detector, light source intensity monitor, and imaging system. The above, except for the light source, are controlled using a computer interface which eliminates the need to interfere with the sample or instruments during the measurement. The components are in three closed compartments, which aim to minimize the amount of stray light from different parts of the system. The compartments, as well as

all feasible parts of the instruments, are coated in black, highly absorbing material preventing reflections. The chambers are isolated from the rest of the room with two overlapping, openable black curtains. The humidity and temperature inside the measurement chamber is constantly monitored, although the practically insulated setup keeps the setting rather constant. The first chamber, containing the optics used to create the light beam, is shown in Figure 4.1, and the second measuring chamber in Figure 4.2.

4.1.1 Light source

The light source and its cooling system are situated outside the chambers to exclude the heat caused by the light source and the turbulence from the fan of the cooling system. The light source is Energetiq EQ-99 Laser Driven Light Source, which produces light covering a broad wavelength range (200–2400 nm). The light is guided into the first chamber through an optical fiber, and the light beam is constructed. In this setup, the light source can be easily replaced without re-aligning the beam. In the first chamber the light is collimated by Thorlabs RC08FC-P01 mirror collimator, after which it passes replaceable Thorlabs laser line filters. The filter has a black square material around it, which prevents extra scattering from subsequent optics. The collimated and filtered light goes to a planoconvex spherical lens ($f = 750$ mm), which focuses the beam. The beam is finally polarized by a motorized birefringent calcite polarizer (Newport 10GL08), before it enters the second chamber where the sample is located.

4.1.2 Sample holder

What makes the 4π scatterometer unique is the sample holder which uses acoustic levitation to levitate the sample mid-air. The sample holder comprises two $\varnothing=15$ cm half spheres, each coated with 222 $\varnothing=10$ mm ultrasonic transducers with a central frequency of 40 kHz and a bandwidth of 1 kHz. The transducers on each hemisphere are further divided into 12 different sections, giving a total of 24 different sections, each comprising multiple transducers. The sections can be controlled individually, which enables complete orientation control of the sample by adjusting the shape of the acoustic field inside the holder. Temperature measurement inside the chamber is crucial for the stability of the levitated sample, as temperature fluctuations affect the shape of the acoustic trap.

The acoustic levitator creates standing waves inside the hemispheres, which

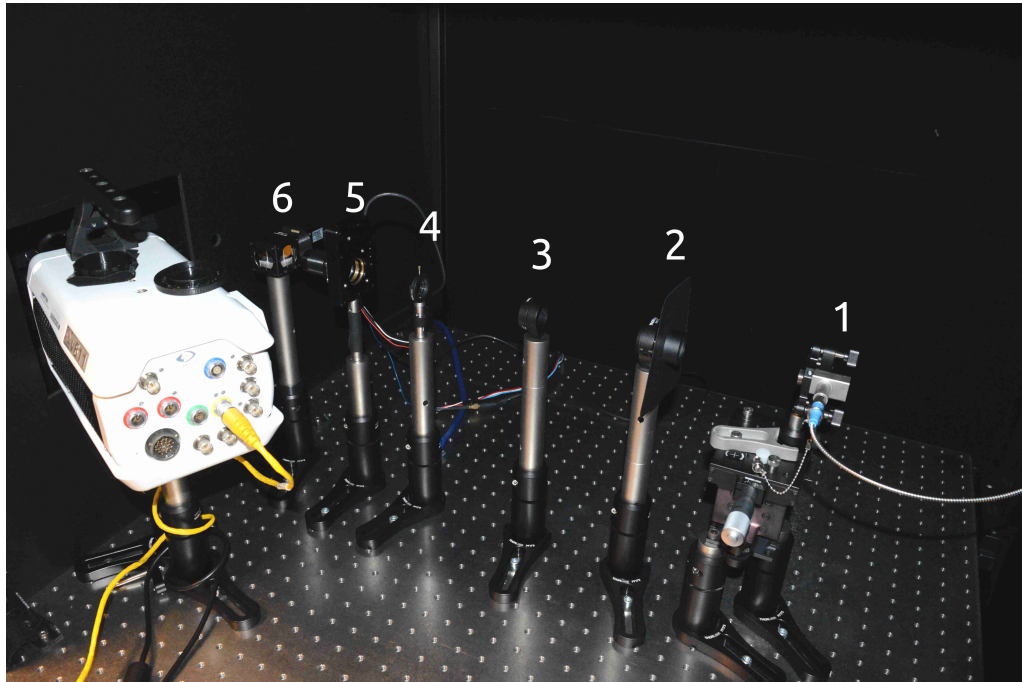


Figure 4.1: The optical setup used for constructing the beam: 1. Collimator 2. Wavelength filter 3. Focusing lens 4. Aperture 5. Polarizer 6. Beam splitter and light source intensity monitor.

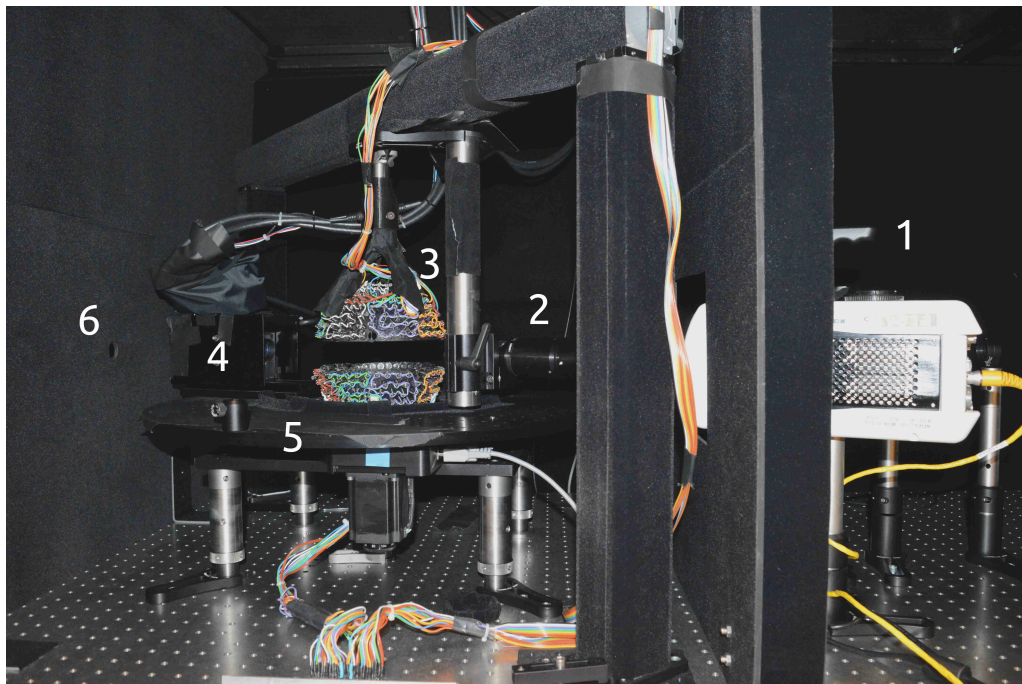


Figure 4.2: The measurement chamber setup: 1. Imaging system camera 2. Microscope objective of the camera 3. Levitator 4. Detector 5. Rotational stage 6. Pinhole to the third chamber.

are adjusted to form an asymmetric potential well where the sample is trapped in place with the largest physical dimension of the sample aligning itself with the axis of the lowest gradient in the potential. The sample orientation can then be controlled by adjusting the trap shape. This enables full control of the samples' rotation around any of its axis (pitch, roll, and yaw). The ultrasonic levitation provides nondestructive measurements and preserves the measured sample in its original state. In a similar measurement setup, the levitator could be switched to a classical sample holder where the object would lay on a pedestal, or for example be glued to a holder. These methods are not feasible for valuable samples, such as those returned from Solar System objects.

4.1.3 Detector

The sensor used in the detector is a Hamamatsu microPMT H12403-01 photomultiplier tube module, connected to a Thorlabs TIA60 amplifier. The sensor is placed in a measurement container with a Thorlabs LPVISE100-A motorized film polarizer and a motorized aperture. The measurement container lies on a $\varnothing=60$ cm circular board, controlled by a Standa 8MRB240-152-59D motorized rotational stage with a resolution of 15'. The detector rotates around the sample, from 0° to 169° . The 11° limitation in the backward direction is caused by the detector crossing the incoming light beam. If angles smaller than 15° are to be used in the forward scattering direction, a neutral density filter should be used in front of the detector to protect it from direct exposure to the high intensity light beam. The mechanized shutter in front of the detector can also be used to adjust the aperture, enabling closer angles to the forward direction without the need of the density filter.

4.1.4 Light source intensity monitor

The intensity of the incoming light is monitored in the first chamber before it reaches the sample. The light source in itself is very stable, but this extra step improves the accuracy of the measurements. Before the polarizer, the light beam is split in two using a beam splitter with the other part continuing to the sample and the other ending up in a PMT sensor, equivalent to that used in the detector, with a neutral density filter at the front.

The intensity of the incoming beam with vertical and horizontal polarizations is monitored in the third chamber, where the beam enters through a small pin hole at the end of the second chamber, using a Newport 918D-UV-OD3R UV Silicon Detec-

tor. This is done to compensate for the possible intensity difference between the two polarization states. These intensity calibration measurements are done separately from the sample measurements, and the sensor in the third chamber is replaced with a beam dampener during the sample measurements to reduce reflections from the beam hitting the lens of the intensity monitor or the wall of the chamber.

4.1.5 Imaging system

The imaging system uses an Phantom v611 hi-speed camera with a microscope objective. The hi-speed camera enables 6242 frames per second at full resolution, and the microscope objective an 120-mm working distance from the lens. The imaging system's primary function is orientation, position, and rotation stability analysis of the sample. This analysis would be best done during the measurements, but specular reflections from the lens of the objective make it usually unfeasible. During the measurements the lens is covered with a filter made from the same black absorbing material the chambers are coated with. The imaging system is turned off during the measurements, as the camera heats up considerably when in use creating heat fluctuations, and the built-in cooling fan causes extra turbulence in the measurement chamber, which both affect the orientation of the sample. The imaging system is controlled individually from a separate computer using Phantom software.

The imaging system can also be used to create a 3D model of the sample, using omnidirectional microscopy. This is done by taking multiple pictures of the sample in different orientations, and then compiling the pictures using a structure-from-motion pipeline. The pipeline creates a 3D point cloud from the sample, which can then be used to create a 3D surface model of the object. Omnidirectional microscopy is further discussed in Chapter 5.2.

4.1.6 Computer interface

The sample holder and detector can be simultaneously controlled from a computer interface on a National Instruments PXIe system. For data acquisition a multi-channel digital oscilloscope (NI PXIe-5171R, 250 MHz, 14 bit) is used to measure the PMT signals, and a general-purpose digital/analog I/O interface (NI USB-6000) is used to read the temperature and humidity sensors. The automation of the measurement process is done with a user interface created in NI LabVIEW. The user interface is used to create an automatic measurement procedure that controls the rotation and the integration time of the detector. The user interface also has

a graphical interface to track the obtained intensity measurements. The input parameters for the user interface are the start and end angles of the measurement, the integration time of one acquisition, the amount of data points, and the number of repeated measurements.

The levitator is controlled using the same computer with a graphical interface built in Pygame. The interface shows how the sample should orient itself in the acoustic trap, based on the sizes of its axis. The orientation can then be rotated in the pitch, yaw, and roll directions. Depending on the material and the asymmetry of the sample, the strength and asymmetry of the trap can be controlled. Generally, more power is needed for heavier objects and more asymmetric trap for more elongated samples. The acoustic power of the trap should be set as low as possible to obtain stable orientation.

4.2 Measurement steps

Before measurements the setup needs about half an hour to warm up and the light source and the temperature in the measurement chambers to stabilize. To achieve highest stability of the sample, the levitator should be calibrated since the shape of the acoustic field is sensitive to variations in temperature, humidity, and air pressure. This is done using an air-coupled transducer with a narrow aperture, with the phase and aperture of each section of transducers on the hemispheres adjusted individually.

Calibration measurements should be taken before and after the sample measurements to check for possible changes during the measurements. The calibration measurements include the intensity measurement of polarization states and measurement of the empty chamber with the light beam on to compensate for specular reflections, ambient light, and electric noise.

The sample is inserted in the levitator using an acoustically transparent mesh. The mesh is made of nylon fabric and doubles as a safety net if the sample is to fall during the measurements. In the acoustic trap, there are multiple potential wells, and the sample needs to be inserted in the correct one which intersects the incoming light beam. After giving the input parameters for the software, the software runs the measurements without further input from the user.

4.2.1 Mueller matrix of the sample

The light scattered from a particle is related to incoming light through the Stokes vector $\vec{S} = (I, Q, U, V)$. The scattering is then described with a 4×4 Mueller matrix \mathbf{M} , as in Equation (2.13). As the detector is situated on the rotating circular board, the distance r remains constant during the measurements. To measure the 16 elements of the scattering matrix, polarizers and quarter wave plates are needed in front of the incident light and the detector. The resulting scattering matrix is a multiplication of the Mueller matrix of individual optical elements the light passes through. If there is a polarizer and a quarter wave plate before and after the sample, the transformation is simply

$$\vec{S}_s = \mathbf{M}_p(\theta_4)\mathbf{M}_q(\theta_3)\mathbf{M}\mathbf{M}_q(\theta_2)\mathbf{M}_p(\theta_1)\vec{S}_i, \quad (4.1)$$

where \mathbf{M}_p is the Mueller matrix of a linear polarizer and \mathbf{M}_q that of a quarter wave plate. The angles θ are the respective angles of polarization of each component. The studied Mueller matrix is \mathbf{M} , which is the effect caused by the particle itself. The Mueller matrix of a linear polarizer and a quarter wave plate are given as,

$$\begin{aligned} \mathbf{M}_p(\theta) &= \begin{pmatrix} 1 & \cos 2\theta & \sin 2\theta & 0 \\ \cos 2\theta & \cos^2 2\theta & \sin 2\theta \cos 2\theta & 0 \\ \sin 2\theta & \sin 2\theta \cos 2\theta & \sin^2 2\theta & 0 \\ 0 & 0 & 0 & 0 \end{pmatrix}, \\ \mathbf{M}_q(\theta) &= \begin{pmatrix} 1 & 0 & 0 & 0 \\ 0 & \cos^2 2\theta & \sin 2\theta \cos 2\theta & \sin 2\theta \\ 0 & \sin 2\theta \cos 2\theta & \sin^2 2\theta & -\cos 2\theta \\ 0 & -\sin 2\theta & \cos 2\theta & 0 \end{pmatrix}. \end{aligned} \quad (4.2)$$

In our setup, only linear polarizers are used. The resulting transformation is then simplified to

$$\vec{S}_s = \mathbf{M}_p(\theta_2)\mathbf{M}\mathbf{M}_p(\theta_1)\vec{S}_i. \quad (4.3)$$

Without the quarter wave plates, the full 4×4 scattering matrix can not be derived, and we are limited to the upper left 2×2 elements; M_{11} , M_{12} , M_{21} , and M_{22} .

The 4π scatterometer does not measure the Stokes vector (\vec{S}_s) values directly. The scatterometer measures intensities I of scattered light in four different polarization configurations from which the Mueller matrix elements can be constructed. To

measure the elements, four different configurations, and measurements are needed:

$$\begin{aligned}
 I_1 : \theta_1 = 0^\circ; \theta_2 = 0^\circ, \\
 I_2 : \theta_1 = 90^\circ; \theta_2 = 90^\circ, \\
 I_3 : \theta_1 = 0^\circ; \theta_2 = 90^\circ, \\
 I_4 : \theta_1 = 90^\circ; \theta_2 = 0^\circ.
 \end{aligned} \tag{4.4}$$

Where θ_1 and θ_2 are the angles of polarization for the polarizers after the light source and before the detector. The final four Mueller matrix elements can be derived from these four measurements:

$$\begin{aligned}
 M_{11} &= I_1 + I_2 + I_3 + I_4, \\
 M_{12} &= I_1 - I_2 + I_3 - I_4, \\
 M_{21} &= I_1 - I_2 - I_3 + I_4, \\
 M_{22} &= I_1 + I_2 - I_3 - I_4.
 \end{aligned} \tag{4.5}$$

4.2.2 Data reduction and accuracy of measurements

The measurement procedure produces the four intensities (I_1 , I_2 , I_3 , and I_4) for different polarization states. The error of the detector is included in the measurement data. To reduce the data, the average value of multiple measurements was first taken. This still includes the possible stray light from the components of the device and the electric noise. The calibration measurements should contain this information and stray light and electric noise are subtracted from the measurement data. If there is a discrepancy between the intensities of the two incoming polarization states, the difference should be taken into account in the measurement and calibration intensities by dividing them with the polarization-calibrated intensity. The final Mueller matrix elements can be calculated as given in Equation (4.5).

Problems in the orientation stability of the sample are not easily reduced from the measurement data, or even quantified. Especially for the heavy glass samples, even small variations in the atmospheric conditions of the measurement chamber correlate to instability of orientation. With multiple measurements the effects of small perturbations should be cancelled out. A considerable problem comes from periodical perturbations of the sample in a particular rotation axis. If the periodic perturbations are present in multiple measurements, they can cause effects to the measured results that are not really present on the sample itself. The best way to tackle the periodic perturbations is to choose a particle orientation that is most stable. The orientation stability of the sample can be quantified using the imaging system. In Helander et al. (2020), the deviations from a desired orientation of

a sample were measured using image detecting software. Unfortunately the main cause for atmospheric variation in the measurement chamber is the imaging system. Orientation stability analysis was not done for the measurements of the glass particles.

5. Laboratory samples

To compare the scattering matrix results from measurements to those from simulations, we used samples with varying shapes, sizes, and refractive indices. The samples were fragments of silicate glass, created as planetary surface analogs by Carli et al. (2016). Silicate glass is a product of volcanism and impact cratering on planetary surfaces, and is a significant contributor to the scattering in visible and near-infrared wavelengths from planetary surfaces (Carli et al., 2016). The samples were suitable to test the pipeline of retrieving the refractive index, as there were four different glassy materials available with slightly different refractive indices, and with fragments of varying shapes. The materials are created from different igneous rock samples and vary in composition, mainly in iron content. They were named by the authors, from the highest iron content to the lowest, Py7, St8, St14, and St18. Of the fragments, three were chosen for every material for 3D modeling, with a total of 12 samples. The original plan was to obtain the refractive index from all of the 12 samples, but ultimately the derivation was done for one particle, as the process proved too laborious for the scope of the thesis. The sample sizes ranged from 1 to 3 mm. There were also prior measurements of the imaginary part of the refractive index of the materials with an integrating sphere, done by A. Penttilä (2022), priv. comm.¹. The igneous rock samples used to produce the glasses are given in Table 5.1.

For the study, the main difference of the samples is in the refractive indices, for which Carli et al. (2016) also derived approximations. They measured the real part of the refractive index using the Brewster angle θ_B . Fresnel equations state that at a certain incidence angle, called the Brewster angle, the light reflected from a boundary is fully polarized. Using polarized incident light, at the Brewster angle all of the parallelly polarized light is transmitted. (Bohren and Huffman, 2008) The Brewster angle depends on the real parts of refractive indices of the two media, here the glass sample (n_2) and air (n_1), by $\theta_B = \arctan(n_2/n_1)$. The measurements were done

¹Penttilä, A. (2022). antti.i.penttila@helsinki.fi

Glass	Original rock sample	n (635 nm)
Py7	Ol-basalt	1.62
St8	Gabbonorite	1.60
St14	Gabbonorite	1.60
St18	Anorthosite	1.58

Table 5.1: The materials of the original rocks the glass samples were produced from, and real parts of the refractive indices (n) of the glasses in 635 nm wavelength, measured in Carli et al. (2016) using the Brewster angle.

using 635-nm red light, and the results are in Table 5.1. For the imaginary part, they used the Hapke model for reflectance spectra described in Hapke (2012), which gives analytical solutions for particulate media. The real part n was approximated to be constant over all wavelengths, and the imaginary part κ was derived by minimizing the difference in measurements and calculations. The reflectance measurements were done on loose grain samples created from the glass materials with different grain sizes. They give the resulting κ -values as a function of wavelength for the different grain sizes, see Figure 5.1.

Measurements on the imaginary part of the refractive index for the glass materials were done in our laboratory using a method by Penttilä et al. (2022). The measurements were done from coarse powders produced by Carli et al. (2016) by grounding the glass samples. Reflectance spectra in 500–2300 nm range were measured from the powders using the Gooch & Housego OL-750 integrating-sphere spectrometer. To derive the imaginary part of the refractive index, the spectra were modeled using a ray-tracing code, and the difference between measurements and model results minimized as a function of κ . A linear extrapolation was done using values in 500 – 550 nm to get a value for the wavelength of 488 nm used in the scatterometer. The derived values for the imaginary parts in 500 and 488 nm are given in Table 5.2 (A. Penttilä, 2022, priv. comm.)².

5.1 3D modeling of laboratory samples

To compare the results to simulations, the shape of the sample fragments were modeled in 3D to be used in the SIRIS4 code. The sample shape was measured by H. Suhonen (2021), priv. comm.³ using X-ray microtomography, which can, using mul-

²Penttilä, A. (2022). antti.i.penttila@helsinki.fi

³Suhonen, H. (2021). heikki.suhonen@helsinki.fi

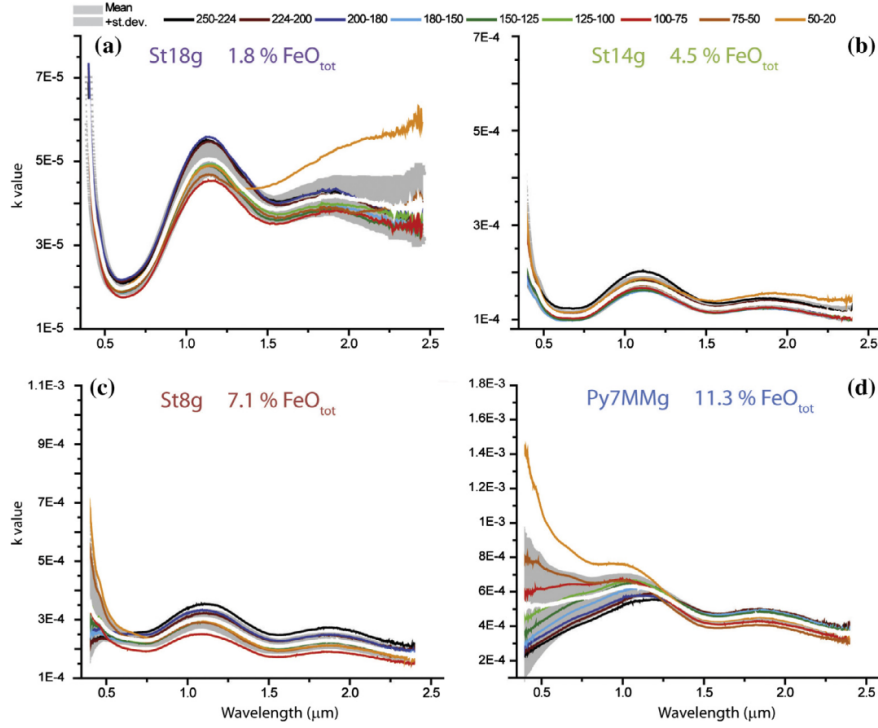


Figure 5.1: Imaginary parts of the refractive indices derived using the Hapke model in Carli et al. (2016), for the four different materials (a) St18, (b) St14, (c) St8 and (d) Py7. The different colors represent different grain sizes, and white the averaged values with its standard deviation in gray.

Glass	κ (500 nm)	κ (488 nm)
Py7	0.0017403	0.00175949
St8	0.000487812	0.000503549
St14	0.000176199	0.000182417
St18	0.0000227323	0.0000233384

Table 5.2: The imaginary parts of the refractive index derived by Penttilä et al. (2022), using an integrating sphere. The 500 nm values are the closest measured values to the wavelength used in the scatterometer measurements, and the 488 nm values have been linearly extrapolated using values in 500 – 550 nm.

multiple measurement angles, capture the shape and internal structure of the sample, from which the triangulated 3D model can be reconstructed. The method of X-ray microtomography is described in Flannery et al. (1987). X-ray microtomography also models the interior of the particle, so the solidity of the particle can be verified. The models produced by the method are accurate to few micrometers, which is beyond the needed accuracy to derive refractive indices from the general shape of the sample. The accuracy is also too high to be used in ray-tracing simulations without needing extensive CPU-times. The models were simplified using automated algorithms available in Meshlab software. The models were first simplified using Quadric Edge Collapse Decimation, and the possible holes in the mesh patched using Surface Construction: Screened Poisson method. The resulting 3D-models had around 5000 faces and 2500 vertices. Examples of the original model and the final model are given in Figure 5.2. The reduced model has $\sim 0.01\%$ of the triangles in the original, but retains the overall shape, positively affecting computation time with SIRIS4. The downside of the reduction in model accuracy is that small surface structure is completely lost, causing possibly small differences in the simulated results compared to the measured. The problems from the simplification can be reduced by choosing samples with relatively smooth surfaces. An example of how the surface structure affects the scattering and how the information about the structure is lost in the simplification is given in Section 7.

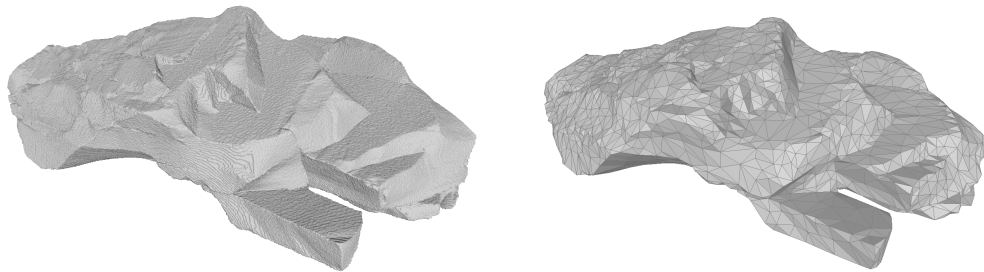


Figure 5.2: Triangulated 3D models of a sample with semi-major axis length of 3 mm. The model on the left has 3000000 faces and 1500000 vertices, and the model on the right has been reduced to 5000 faces and 2500 vertices.

5.2 Omnidirectional microscopy

Before choosing X-ray microtomography as the modeling method for the shape, omnidirectional microscopy was attempted, which uses only the scatterometer itself,

detailed in Helander et al. (2020). In their method, 3×120 images of the sample were taken with 3° increments over the main rotation axis. The images were then reconstructed using a structure-from-motion (SfM) pipeline. SfM detects common features between the images and finds the correct camera angles around the sample. In the imaging system, the camera is stationary while the sample rotates around its axis, which is analogous to the camera rotating around a stationary sample. The SfM pipeline assumes that the sample is stationary and the pictures are taken around the sample. SfM generates a 3D point cloud from the target, which can then be used to create a 3D surface model using mesh processing software.

As Helander et al. (2020) point out, the challenges in creating a 3D model using omnidirectional microscopy come from a sample not having a perfect Lambertian reflection and not enough surface texture to find common features between the images. Surface texture could be artificially added to the sample by, e.g., drawing on it, but this is obviously not suitable for the purposes of light scattering studies. Additionally, SfM is not suitable for transparent objects as the algorithm is not able to distinguish surface reflections from those coming from inside the sample. Despite the limitations, omnidirectional microscopy was tried for modeling of the most opaque samples. The method ultimately proved insufficient for the glassy samples used in this study but is a valuable tool in the future, for example for opaque rock samples, constraining the whole measurement procedure to only one device.

6. Measurements

6.1 Calibration measurements

Before constructing the new SIRIS4 FO simulation, the SIRIS4 single-particle software was used to validate the method of comparing scatterometer measurements to computer simulations. The single-particle code gives the scattering results averaged over random particle orientations, so the results could not be compared to measurements using fixed orientation. As a first test for the measurements, a matte-surfaced glass sphere was used. A symmetric spherical particle gives the same scattering results regardless of the orientation, so the averaging does not affect the results. The matte surface is caused by micro roughness on the surface of the glass, which could cause different scattering effects on specific measurement angles, and ruin the symmetry. This is counteracted by the sphere not being stable in the acoustic trap and spinning rapidly during the measurements.

The measured particle was a 3-mm sized N-BK7 glass sphere with a matte surface. To model the matte-surfaced sphere in SIRIS4, a similar model sphere was created using the Gaussian particle generator within the SIRIS4 framework, which eliminates the need for a precise modeling of the sample. The Gaussian sphere in SIRIS4 is defined with 4 parameters: the standard deviation of radial distance, the power law index for correlation, the maximum degree in the correlation series, and the number of triangle rows per octant on the sphere. The values used for the frosted sphere were 0.01, 0.1, 60, and 30. The model produced was a sphere with very fine surface roughness. The size deviation of the surface roughness did not affect the results much in the used size range, and the particle shape model proved to be sufficient. The sample and the Gaussian 3D model are shown in Figure 6.1.

The refractive index of the N-BK7 glass is well documented (at $\lambda = 488$ nm, $m = 1.52 + i 9.8 \cdot 10^{-9}$ (Schott Advanced Optics, 2023)), and the Gaussian sphere was ran in SIRIS4 single-particle code to obtain orientation-averaged results. The input parameters used in SIRIS4 single-particle are given in Table 6.1. The results

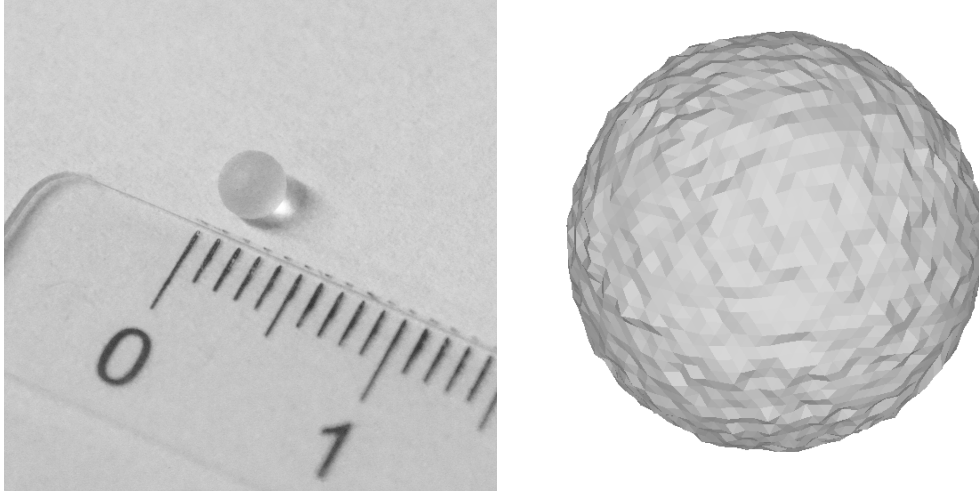


Figure 6.1: On the left the matte surfaced N-BK7 glass sphere used in the scatterometer. On the right is a Gaussian random particle model that mimicks the matte surface on the glass sphere.

of the measurements and SIRIS4 are given in Figure 6.2. The S_{11} elements are normalized to provide meaningful comparison between the two. The measurements and simulation follow each other remarkably well. The SIRIS4 simulation was used as a calibration point for the measurements, and the likeness of the measurements to the simulated data prove that the measurements work at the desired accuracy.

SIRIS4 single-particle input parameters	
Number of rays	10^5
Number of sample particles	1
Minimum relative flux	10^{-4}
Max internal chord	21
Min internal chord	21
Number of scattering angle bins	60
Particle refractive index, real	1.52
Particle refractive index, imaginary	$9.8 \cdot 10^{-9}$
Seed for random number generation	0
Wavelength (micrometers)	0.488
Mean radius (micrometers)	2500

Table 6.1: SIRIS4 single-particle input parameters used in the simulation of the N-BK7 glass sphere with a matter surface.

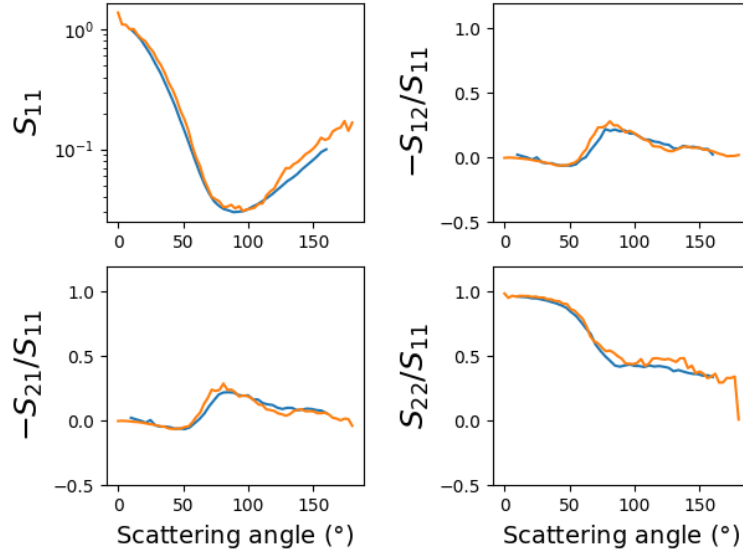


Figure 6.2: Scattering matrix elements as a function of scattering angle for a matte surfaced N-BK7 glass sphere. The blue lines describe the measured values and the orange lines those from SIRIS4.

6.2 Random orientation

The measurement process was validated with the use of a spherical particle. To validate the whole pipeline of measuring a sample and translating its 3D model to SIRIS4, random-orientation measurements were used. In measurements, random orientation can be achieved by taking measurements of a particle in different orientations or from a collection of randomly orientated particles.

The levitator in the 4π scatterometer is originally built with controlled orientation in mind, but can be extended to random orientation. There are two ways to approach this, either take multiple measurements of the sample in different orientations, or rotate the sample during the measurements. Both of the ways require manual manipulation of the orientation of the particle. Producing truly randomized orientations manually is difficult, as it is hard to guarantee that no particular orientation is favored. A solution was found by increasing the amplitude of the acoustic trap, thus making it unstable. This causes the sample to spin rapidly and chaotically inside the acoustic field.

A St18 glass particle, the 3D model of which is shown in Figure 5.2, was used for the process. Different ways to measure random orientation were tried for the sample. The sample was first measured in multiple different stationary orientations. Even with 20 orientations, the results did not converge to those obtained from SIRIS4, and

randomly orientating particles manually was found not to be sufficient. The best way to measure random orientation is to achieve chaotic random orientation. Using our levitator, this would be feasible for less dense objects that have a somewhat spherical shape. The properties of the sample particle, being dense and elongated, cause the particle to always rotate around a particular axis. This rotation symmetry could be broken by increasing the amplitude of the acoustic trap, causing the sample to rotate unexpectedly. This in turn causes instability in the levitation, with the sample easily falling off of the trap. A middle ground was found by increasing the amplitude slightly which causes the particle to rotate around a specific axis multiple times during one detector integration. The orientation of the axis of rotation was then changed after every measurement to produce a semi-randomly rotating particle.

SIRIS4 single-particle code was then run using the 3D model of the particle measured in random orientation. As the input parameters defining the particle, SIRIS4 needs the mean size of the particle and its refractive index. The size of the particle was measured using a ruler. For refractive index, the values obtained by the authors in Carli et al. (2016) were used. For the other input parameters, the same values as for the N-BK7 glass sphere were used, given in Table 6.1.

The comparison of the measurements to SIRIS4 was done multiple times, and after each, more semi-random measurements were taken. With around 20 measurements in total, the average of the measurement results started to converge to those of SIRIS4. The final results from 20 measurements and from SIRIS4 are shown in Figure 6.3. There are errors in the measurements, but the overall trend in the scattering matrix elements follow the simulations. The errors are credited to the method of obtaining the random orientation. It is feasible to say that the results from SIRIS4, using the refractive index provided by the manufacturer of the glass, are similar to the measurements of the particle, and the 3D modeling of the particles is sufficient. The study was then conducted further with measurements of the particles in a fixed orientation and the creation of the new SIRIS4 FO code.

6.3 Fixed orientation

Using randomly orientated particles, the SIRIS4 single-particle code was used to validate the measurements. When the single-particle code was modified to the SIRIS4 FO method, the measurements in fixed orientation with the scatterometer could be used to validate the newly created code. Fixed orientation measurements were done on multiple particles and glasses to gather enough references to which the SIRIS4

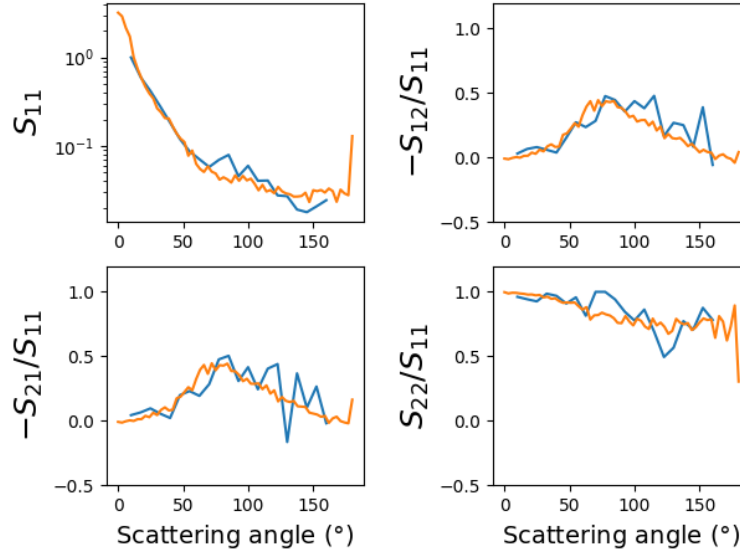


Figure 6.3: Scattering matrix elements as a function of scattering angle for a sample of St18 glass. Blue lines present the measured values obtained as an average of multiple semi-random orientations. The orange lines are the results derived from SIRIS4 single-particle.

FO results could be compared to. The 4π scatterometer is specifically built to levitate particles in a fixed position and orientation, and with the scatterometer the fixed orientation measurements are easier to do and require less work than those done with random orientation.

The glassy particles used in the study are difficult objects to levitate, because of their high density. The acoustic trap does not take gravity into account in its calculations. This causes the particles to be tilted towards the ground on the heavier side of the elongated particle, with the consequence that all orientations are not stable. The measurements needed to be done first to find a stable orientation, and afterwards the particle and orientation translated to SIRIS4. Even the most stable orientations still had some vibration on the particle. The vibrations were often systematic in a specific direction, which causes systematic error in all of the measurements and would not be canceled out in averaging multiple results. Fortunately, the angular bin size in the simulations is a restricting factor and averages out the small vibrations. If scattering is to be studied with a larger angular resolution, the particle vibration needs to be resolved. The vibrations could be quantified and analyzed with the imaging software and high-speed camera, but is too laborious to be done in this study.

There is a large difference between the stabilities of different particles. As many particles were levitated in fixed orientation to be used as references when

constructing the SIRIS4 FO, a few suitable particles for which a specific levitation orientation was extremely stable stood out. One of these particles of St18 glass was chosen, for which the final refractive index determination was done. Another positive property of the particle were the smooth surfaces, which meant that not a lot of information was lost in the simplification of the 3D model. The particle had multiple sharp corners which produce noticeable effects to the scattering matrix elements and help to constrain the right orientation of the model in SIRIS4 FO. Six measurements from the particle were made in $10^\circ - 160^\circ$ range with 40 data points, which corresponds to 3.75° angle resolution. Another six calibration measurements were taken after the measurements. The average of six measurements is adequate to cancel out small effects caused by possible turbulence in the chamber which can affect measurements. More measurements do not necessarily improve the results as the atmospheric properties of the chamber change slowly.

7. Results for complex refractive index

The measurements from the 4π scatterometer provide the data of the real scattering behavior of the particle. The parameters defining the scattering can be derived by comparing the measurements to light scattering simulations in which the parameters can be varied. The accuracy of the derivation depends heavily on the accuracy the particle and scattering effects can be modeled in simulations. As SIRIS4 code is used, the variables defining the scattering are the 3D model of the scatterer, the orientation of the scatterer in the model, the scatterer size, and the complex refractive index. To determine the refractive index, the other parameters need to be known a priori. SIRIS4 FO reads the size of the particle directly from the file of the 3D model. The size is read in micrometers, so the 3D model should contain this information in the correct units. The orientation of the particle should be translated to the model using the particle coordinate system. The orientation analysis in the study was done by eye using the imaging system of the scatterometer. The orientation is thus not exact in the simulations. The orientation of the particle was further iterated a bit, by running SIRIS4 with multiple orientations with small deviations from the original. The complex refractive index derived by Carli et al. (2016) was used, and the best results for the orientation chosen. The final problems caused by the 3D model come from the simplification of the model. To calculate the scattering effects in a reasonable amount of time, the models had to be considerably simplified, which does not largely affect the overall shape of the model but does remove possible surface texture.

A clear example of how the simplification of the model affects the results is seen in one particular particle of St8 glass. Rough first model between the measured and simulated scattering elements is given in Figure 7.1. In the S_{11} and S_{22}/S_{11} elements, the simulations seem to match the measurements well in $0^\circ - 90^\circ$, compared to the precision of the iteration. In $90^\circ - 160^\circ$, there is a large discrepancy between the two

elements. In the backscattering region, the S_{11} element shows scattering intensity familiar to those from asteroid observations. In the backscattering direction, the sample gets brighter as the effect of rough surface shadowing disappears (Capaccioni et al., 1990). The brightening effect is not simulated properly by SIRIS4. One reason for the difference comes from the simplification of the 3D model. As to the backscattering regime, the particle has small surface texture which seems to mimic small loose particles on the surface of an asteroid. The simplification process smooths out these surface imperfections, as can be seen in Figure 7.2, and SIRIS4 is not able to reproduce the effect.

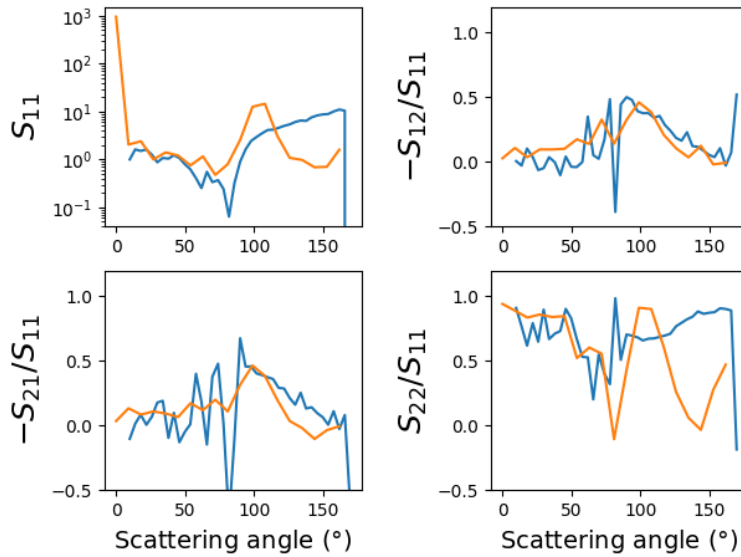


Figure 7.1: Scattering matrix elements as a function of scattering angle for a sample of St8 glass. The glass particle has small surface roughness, which can be seen affecting the measurements (blue), but is not correctly translated to the measurements (orange). The discrepancies present in the measurements in the backscattering regime ($\sim 160^\circ$) are caused by the detector blocking the light source.

With other simulation parameters chosen, which are given in Table 7.1, SIRIS4 FO was run with different values of the refractive index to obtain results the measurements could be compared to. The values of the refractive index were chosen around the result derived by Carli et al. (2016). The real part was iterated in $n = 1.44 - 1.78$ with 0.01 intervals and the imaginary part in $\kappa = 10^{-3} - 10^{-6}$ with gradually increasing intervals by incrementing the exponent by 0.1. SIRIS4 calculates also the forward and backscattering parts of the scattering matrix, which are out of the reach of the scatterometer. Measurement points that are out of the measurement range of the scatterometer were removed from the S_{11} element to provide

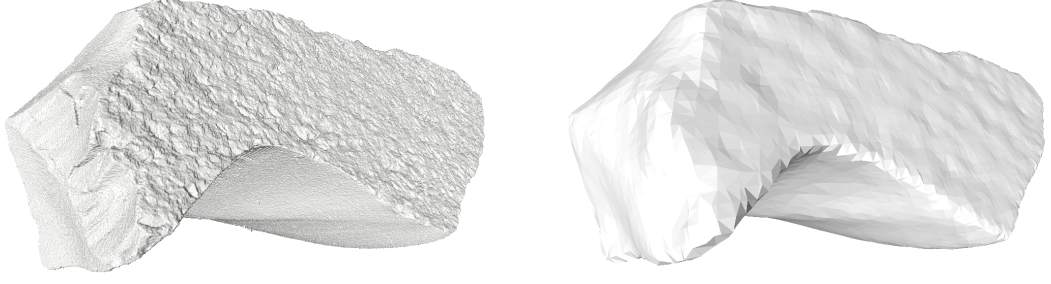


Figure 7.2: 3D models of a particle of St8 glass. On the left the model produced by X-ray microtomography, and on the right a simplified version used in SIRIS4. The original model shows the small surface texture present on one side of the particle. The simplification process loses the information on the surface texture, which strongly affects scattering.

a better visual comparison between the two elements, as there is otherwise a large spike present in the forward scattering part. As the simulation and scatterometer give intensity in arbitrary units, the S_{11} elements are not directly comparable. To compare the elements, all the points of S_{11} from simulations and measurements were divided by the average value of the element.

SIRIS4 FO input parameters	
Number of rays	10^5
Number of sample particles	1
Minimum relative flux	10^{-4}
Max internal chord	21
Min internal chord	21
Number of polar scattering angle bins	36
Number of azimuthal scattering angle bins	36
Seed for random number generation	0
Wavelength (millimeters)	0.000488

Table 7.1: SIRIS4 FO input parameters used in the derivation of the refractive index. Compared to SIRIS4 single-particle, in SIRIS4 FO the number of azimuthal scattering angle bins needs to be defined. The mean radius of the particle is read directly from the 3D model in millimeters, and the wavelength needs to be given in millimeters as well.

The results from the simulations show a few differences from the measured elements that are present in every iteration. An example of one iteration with a refractive index of $m = 1.58 + i1.5 \cdot 10^{-5}$ is given in Figure 7.3. From the figure, three inconsistencies that cannot be credited to random noise are visible. In the S_{11} element, the simulated values are lower near the backscattering direction, around

$100^\circ - 160^\circ$. In the $-S_{12}/S_{11}$ and $-S_{21}/S_{11}$ elements, there is a spike near forward scattering ($10^\circ - 30^\circ$). Lastly in the S_{22}/S_{11} element, the end in $130^\circ - 160^\circ$ in the backscattering regime gives smaller values than the measurements. All three problems were systematic differences present in every iteration of the simulations and no simple explanation for the cause was found. The causes for the inconsistencies are probably the sum of imperfect translation of orientation to SIRIS4 FO, the simplification of the 3D model, and the way the resolution in the ϕ -binning is chosen. How the resolution for the ϕ -binning is chosen defines the area on the surface of the particle from which the imaginary detector in the simulation measures scattering effects. The 10° ϕ -angle coverage present in the simulations is more than the detector angular area in the scatterometer measures. SIRIS4 averages the scattering over the detection area of a single bin, and a smaller bin count can cause effects to a viewing angle that are not visible in the measurements.

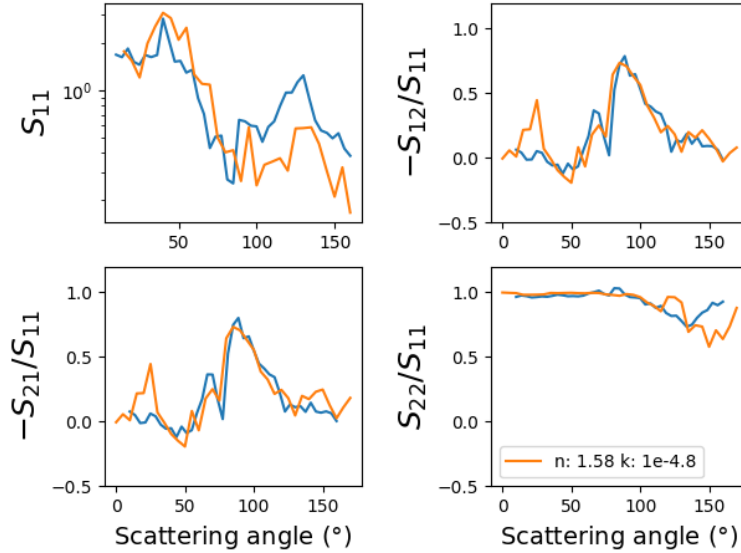


Figure 7.3: Comparison on simulations (blue) to measurements (orange), with a complex refractive index value of $m = 1.58 + i1.5 \cdot 10^{-5}$. The two graphs show remarkable likeness to each other, except for a few outliers, which are credited to the translation of the scattering particle to SIRIS4.

Non-linear least squares analysis by Benšić (1997), and adopted by A. Penttilä (2022), priv. comm.¹, is used to quantify the likeness of the measurements and simulations, and to derive confidence intervals for the results. The method works by finding a vector $\vec{m} = (n, \kappa)$ that minimizes the sum of squared residuals. To quantify the errors that come from the shape and orientation of the 3D model would require

¹Penttilä, A. (2022). antti.i.penttila@helsinki.fi

rigorous analysis on how the two variables affect the simulation results. In the analysis, the residuals are estimates of the random errors in the nonlinear model. The residuals $\vec{e} = e_1, \dots, e_N$ are given as,

$$\vec{e} = \vec{y} - \vec{f}(\vec{m}), \quad (7.1)$$

where $\vec{y} = y_1, \dots, y_N$ are the measured values and $\vec{f}(\vec{m}) = f_1, \dots, f_N$ the simulation results with two free parameters $\vec{m} = (n, \kappa)$. The sum-of-squared-errors (SSE) is then

$$S(\vec{m}) = \sum_{i=1}^N e_i^2 = \sum_{i=1}^N (y_i - f_i(\vec{m})). \quad (7.2)$$

The SSE is then compared to a model which minimizes the SSE, called $S(\hat{\vec{m}})$ and a value quantifying every combination of refractive index real and imaginary parts is found $S(\vec{m})/S(\hat{\vec{m}})$.

In Figure 7.4, the $S(\vec{m})/S(\hat{\vec{m}})$ values are plotted as a function of the real and imaginary parts of the refractive index, for the scattering matrix elements S_{11} , $-S_{12}/S_{11}$, and S_{22}/S_{11} , with smaller values corresponding to a greater likeness between measurements and simulation. Each of the three elements define upper boundaries for the imaginary part of the refractive index κ , but only the S_{22}/S_{11} element, which describes depolarization, gives also a clear lower boundary, defining the value of κ only, without giving any information on the real part n . This is expected, as can be seen from Equation (2.14). The light incident on a particle is completely confined to the amplitude scattering matrix (2.11) elements S_1 and S_2 . If κ is high for the material, the light is scattered from the surface, and the S_3 and S_4 values stay close to zero. With a smaller κ value, the incident light ray scatters multiple times inside the particle, causing changes to polarization and rise to the S_3 and S_4 values, which is then seen in the depolarization value. In Figure 7.4c, it can be seen that the best values are constrained to a straight line around $\kappa = 10^{-4.4}$, but that there are values with a smaller imaginary part outside this line that give good results. These outliers are credited to the imprecision of the SIRIS4 FO simulations. With a relatively low ray-count in the simulations, the results have some variation, which causes the outliers. The same behavior affects all of the elements, which is why the results are treated as trends instead of individual data points. A value for κ can be found from the depolarization (S_{22}/S_{11}) element, and afterwards the real part n can be derived from the intensity (S_{11}) and degree of linear polarization (S_{12}/S_{11}) elements. With just any of the elements alone, the complex refractive index could not be confined fully. The results demonstrate well the importance of

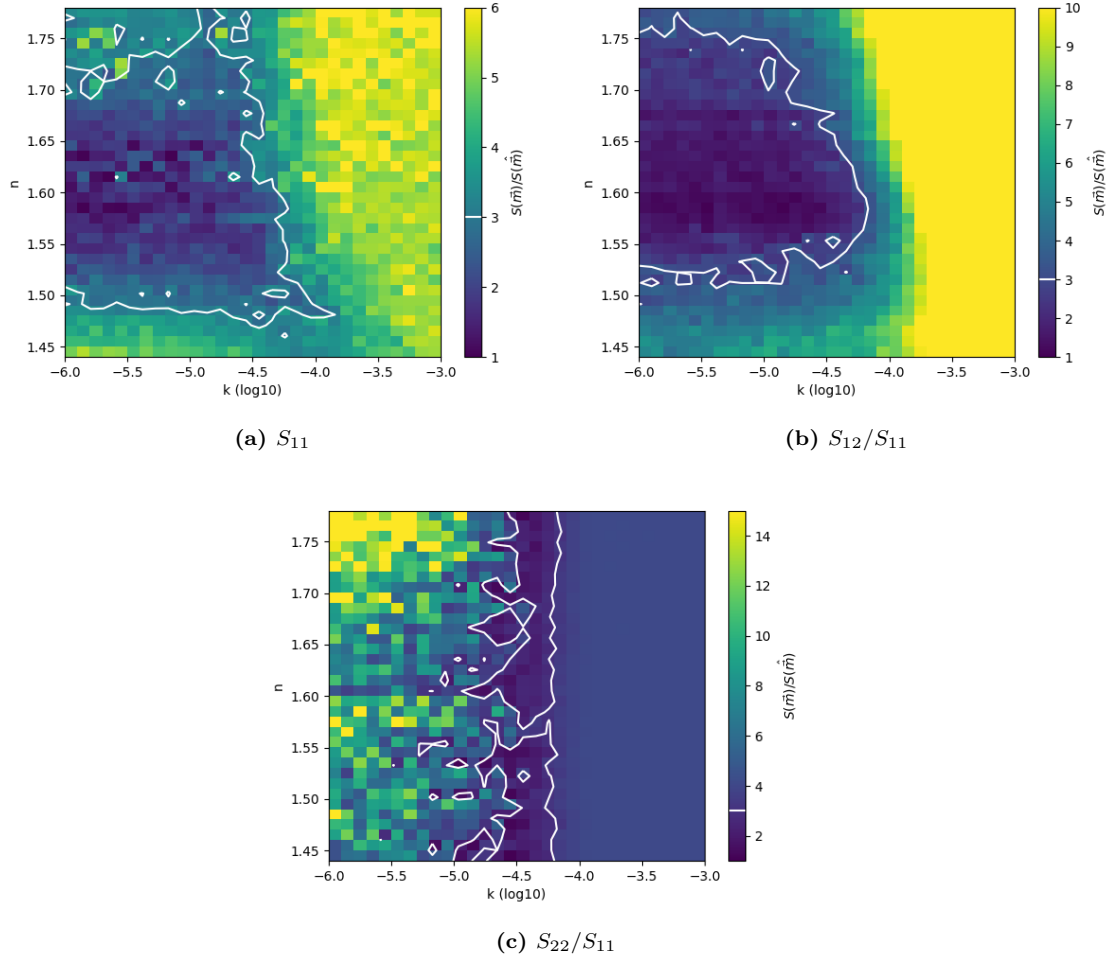


Figure 7.4: $S(\vec{m})/S(\hat{\vec{m}})$ values of scattering elements as a function of the refractive index real part n and imaginary part κ . Smaller values correspond to a greater likeness between the simulations and measurements. The plotted white contour gives an area where $S(\vec{m})/S(\hat{\vec{m}}) \leq 3$. A linear trend can be seen in the S_{22}/S_{11} element, which constrains the value for κ . S_{11} and S_{12}/S_{11} elements constrain the value for n , but give only upper boundaries for κ .

using polarized light and measuring the Mueller matrix elements instead of just the intensity of scattered light.

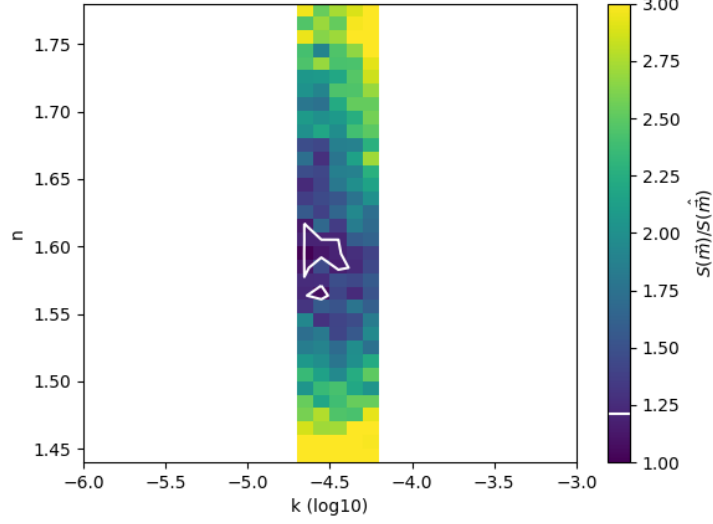


Figure 7.5: Combined $S(\vec{m})/S(\hat{\vec{m}})$ values for all three (S_{11} , S_{12}/S_{11} , S_{22}/S_{11}) of the elements calculated in the interval from $\kappa = 10^{-4.8} - 10^{-4.3}$. The white contour gives the 99.9% confidence interval for the results.

$\lambda = 488 \text{ nm}$	
n	1.59 ± 0.02
κ	$2.05 \pm 0.46 \cdot 10^{-5}$

Table 7.2: The final derived real (n) and imaginary (κ) parts of the complex refractive index using $\lambda = 488 \text{ nm}$ wavelength.

From the derived $S(\vec{m})/S(\hat{\vec{m}})$ value, confidence regions for the model likeness can be calculated [A. Penttilä, 2022, priv. comm.]². The $(1 - \alpha) \%$ confidence region for \vec{m} is a region where,

$$\frac{S(\vec{m})}{S(\hat{\vec{m}})} \leq 1 + \frac{N_m}{N - N_m} \mathcal{F}(1 - \alpha; N_m; N - N_m), \quad (7.3)$$

where N_m is the amount of free parameters in the model (here 2), and $\mathcal{F}(1 - \alpha; N_m; N - N_m)$ the value of inverse cumulative distribution function of the F-distribution at $1 - \alpha$. The method does not fully explain the errors between the measurements and simulations, and gives very small confidence regions. The small

²Penttilä, A. (2022). antti.i.penttila@helsinki.fi

confidence regions should not be trusted as the simulation accuracy is not well confined in the presumed errors of the model. Because the S_{22}/S_{11} element confines the value of the imaginary part κ well, it is first used to give an interval for κ from which the combined effect of all elements can be calculated. By choosing an interval for κ first, most of the outliers resulting from simulation inaccuracies are removed. A generous confidence interval is used with the S_{22}/S_{11} element of $S(\vec{m})/S(\hat{\vec{m}}) \leq 3$ (which corresponds to a 99.999999 % confidence interval), to get some information of the relevant regions in (n, κ) -space. The confidence interval is plotted as a white contour in Figure 7.4c. From the figure, it can be said with high confidence that the value for κ should be inbetween $\kappa = 10^{-4.8}$ and $\kappa = 10^{-4.3}$, where there is a straight line trend present. To derive a final result for the complex refractive index, a combined SSE of all three elements was calculated in the $\kappa = 10^{-4.8} - 10^{-4.3}$ region. The combined SSE ($S(\vec{m})$ in Equation (7.2)) was constructed by summing the individual SSEs of the S_{11} , S_{12} , and S_{22} elements

$$S(\vec{m}) = S_{11}(\vec{m}) + S_{12}(\vec{m}) + S_{22}(\vec{m}). \quad (7.4)$$

The $S(\vec{m})/S(\hat{\vec{m}})$ values for the combined model, and the values inside a 99.9 % interval are given in Figure 7.5. There is an outlier region below the larger confidence region, which is ignored as it is caused by only one simulation result. The middle point of the values that fit in the larger area defined by the 99.9 % interval is chosen as the final value of the complex refractive index. The final results are given in Table 7.2.

The $n = 1.58$ value for the real part, derived in Carli et al. (2016) and given in Table 5.1, and the imaginary part $\kappa \sim 2.5 \cdot 10^{-5}$ (inferred by eye from Figure 5.1) fit in the confidence region of our results. The imaginary part value $\kappa = 2.33 \cdot 10^{-5}$ derived by Penttilä et al. (2022), given in Table 5.2, also supports our findings.

8. Conclusions

In the thesis, the refractive index of a mm-sized single glass particle was derived successfully with the 4π scatterometer using fixed orientation. The measurements were done from an acoustically levitated particle, which can be orientationally controlled. The measurements were compared to simulations from a newly created SIRIS4 FO light scattering code. The complex refractive index values were varied in the simulations, and the results were compared to measurements. The refractive index values that give the best fit to the measurements were deduced as the correct refractive index values for the sample.

The SIRIS4 light scattering codes calculate the scattering matrix elements averaged over the orientation of the particle. To compare the simulations to measurements from the scatterometer in fixed orientation, the SIRIS4 single-particle implementation was modified to use particles in a fixed orientation, producing the new version SIRIS4 Fixed Orientation (FO). In SIRIS4 FO the orientation of the particle in respect to the laboratory coordinates needs to be defined in the input using Euler angles. SIRIS4 FO calculates the scattering matrix elements over the full solid angle around the particle.

SIRIS4 reads the shape of the scattering particle from a 3D model given as input. The particle measured in the scatterometer was 3D-modeled using X-ray microtomography. The resulting 3D model had an accuracy of few micrometers which is too accurate to be used in SIRIS4 simulations due to high computing times. The 3D model was simplified using automated algorithms in Meshlab software. The resulting 3D model loses information about the surface texture of the particle, causing discrepancies between the simulated and measured results. This was counteracted by choosing particles with relatively smooth surfaces.

The 4π scatterometer uses an acoustic levitator as a sample holder. Acoustic levitation provides nondestructive measurements and full orientation control of samples. The scattering matrix elements are measured from the particle using linear polarizers and a detector rotating about the particle on a rotational stage. Mea-

measurements were first done on particles in semi-random orientation in the scatterometer to produce orientation-averaged scattering. The orientation-averaged scattering measurements closely resemble those from SIRIS4 single-particle simulations. The orientation-averaged SIRIS4 simulations could also be used to determine the refractive index of samples by taking orientation-averaged measurements. Measurements from fixed orientation were used in the study, as the scatterometer is specifically built to handle particles in fixed orientation.

SIRIS4 FO was ran with multiple different values of the complex refractive index to produce differing scattering matrix results. The comparison of scattering matrix results from simulations to measurements was done using nonlinear least squares analysis by finding the real and imaginary parts of the complex refractive index that minimize the sum of squared residuals between the measurements and simulations. The errors in the simulations mainly come from the simplification of the 3D model of the sample and the orientation translated from measurements, and are thus hard to quantify. Confidence regions could be derived for the results, by estimating the residuals as the random errors in the non-linear model. Using 488 nm light, the refractive index of St18 glass particle was derived to be $m = 1.59 \pm 0.02 + i 2.05 \pm 0.46 \cdot 10^{-5}$, with a 99.9% confidence.

For future work, there are multiple improvements to be done in the measurement pipeline to produce more accurate results faster. One is the ongoing process of installing multiple detectors on the 4π scatterometer to be used simultaneously, which reduces the measurement time, improving the measurement accuracy. The discrepancies that arise from the orientation of the 3D model could be minimized by measuring the orientation of the particle during the measurements using the scatterometer imaging system and an automated pipeline. The imaging system could also be used to quantify the errors in the sample orientation during the measurements by constantly imaging the sample and recording its orientation fluctuations. The last action to easily improve the pipeline is to use more computing power for the simulations. The simplification on the 3D model of the particle would not have to be as coarse and the angular resolution in the simulations could be higher.

For the first time, scattering matrix results from a measurement of levitated mm-sized particle in fixed orientation were compared to light scattering simulations. The complex refractive index of a glass particle was derived successfully, and a new pipeline was created to produce such measurements of the refractive index. The available comparison of simulations to real measurements in fixed orientation is also in itself a valuable tool in light scattering studies.

Bibliography

- Benšić, M. (1997). Confidence regions and intervals in nonlinear regression. *Mathematical Communications (mc@mathos.hr)*; Vol.2 No.1.
- Bohren, C. F. and Huffman, D. R. (2008). *Absorption and Scattering of Light by Small Particles*. Wiley-VCH, New York, 1. Aufl. edition.
- Born, M. (1999). *Principles of optics : electromagnetic theory of propagation, interference and diffraction of light*. Cambridge University Press, Cambridge, 7th (expanded) ed. edition.
- Capaccioni, F., Cerroni, P., Barucci, M., and Fulchignoni, M. (1990). Phase curves of meteorites and terrestrial rocks: Laboratory measurements and applications to asteroids. *Icarus*, 83(2):325–348.
- Carli, C., Roush, T., Pedrazzi, G., and Capaccioni, F. (2016). Visible and near-infrared (vnir) reflectance spectroscopy of glassy igneous material: Spectral variation, retrieving optical constants and particle sizes by hapke model. *Icarus*, 266:267–278.
- Chang, P. C., Walker, J., and Hopcraft, K. (2005). Ray tracing in absorbing media. *Journal of Quantitative Spectroscopy and Radiative Transfer*, 96(3):327–341.
- Flannery, B. P., Deckman, H. W., D’Amico, K. L., and Roberge, W. G. (1987). Three-dimensional X-ray microtomography. *Science*, 237:1439–1444.
- Fox, M. A. M. (2010). *Optical properties of solids*. Oxford master series in physics ; 3. Condensed matter physics. Oxford University Press, Oxford ;, second edition. edition.
- Frezza, F., Mangini, F., and Tedeschi, N. (2018). Introduction to electromagnetic scattering: tutorial. *J. Opt. Soc. Am. A*, 35(1):163–173.

- Griffiths, D. J. D. J. (2017). *Introduction to electrodynamics*. Cambridge University Press, Cambridge, fourth edition. edition.
- Hansen, J. E. and Travis, L. D. (1974). Light scattering in planetary atmospheres. *Space Science Reviews*, 16(4):527–610.
- Hapke, B. (2012). *Theory of Reflectance and Emittance Spectroscopy*. Cambridge University Press, 2 edition.
- Helander, P., Puranen, T., Meriläinen, A., Maconi, G., Penttilä, A., Gritsevich, M., Kassamakov, I., Salmi, A., Muinonen, K., and Hægström, E. (2020). Omnidirectional microscopy by ultrasonic sample control. *Applied Physics Letters*, 116(19):194101.
- Holland, A. C. and Gagne, G. (1970). The scattering of polarized light by polydisperse systems of irregular particles. *Appl. Opt.*, 9(5):1113–1121.
- Hovenier, J. and Muñoz, O. (2009). Light scattering in the solar system: An introductory review. *Journal of Quantitative Spectroscopy and Radiative Transfer*, 110(14):1280–1292. XI Conference on Electromagnetic and Light Scattering by Non-Spherical Particles: 2008.
- Hunt, A. J. and Huffman, D. R. (1973). A new polarization-modulated light scattering instrument. *Review of Scientific Instruments*, 44(12):1753–1762.
- Kassamakov, I., Maconi, G., Penttilä, A., Helander, P., Gritsevich, M., Puranen, T., Salmi, A., Hægström, E., and Muinonen, K. (2018). Light scattering by ultrasonically-controlled small particles: system design, calibration, and measurement results. In Soskind, Y. G., editor, *Photonic Instrumentation Engineering V*, volume 10539, page 105390R. International Society for Optics and Photonics, SPIE.
- Kemppinen, O., Nousiainen, T., Merikallio, S., and Räisänen, P. (2015). Retrieving microphysical properties of dust-like particles using ellipsoids: The case of refractive index. *Atmospheric Chemistry and Physics*, 15:11117–11132.
- Kuik, F., Stammes, P., and Hovenier, J. W. (1991). Experimental determination of scattering matrices of water droplets and quartz particles. *Appl. Opt.*, 30(33):4872–4881.

- Lindqvist, H., Martikainen, J., Rabinä, J., Penttilä, A., and Muinonen, K. (2018). Ray optics for absorbing particles with application to ice crystals at near-infrared wavelengths. *Journal of Quantitative Spectroscopy and Radiative Transfer*, 217:329–337.
- Long, L., Querry, M., Bell, R., and Alexander, R. (1993). Optical properties of calcite and gypsum in crystalline and powdered form in the infrared and far-infrared. *Infrared Physics*, 34(2):191–201.
- Lucey, P. G. (1998). Model near-infrared optical constants of olivine and pyroxene as a function of iron content. *Journal of Geophysical Research: Planets*, 103(E1):1703–1713.
- Maconi, G., Helander, P., Gritsevich, M., Salmi, A., Penttilä, A., Kassamakov, I., Hægström, E., and Muinonen, K. (2020). 4π scatterometer: A new technique for understanding the general and complete scattering properties of particulate media. *Journal of Quantitative Spectroscopy and Radiative Transfer*, 246:106910.
- Maconi, G., Kassamakov, I., Penttilä, A., Gritsevich, M., Hægström, E., and Muinonen, K. (2017). Experimental light scattering by small particles: system design and calibration. In Lehmann, P., Osten, W., and Jr., A. A. G., editors, *Optical Measurement Systems for Industrial Inspection X*, volume 10329, page 103292S. International Society for Optics and Photonics, SPIE.
- Maconi, G., Penttilä, A., Kassamakov, I., Gritsevich, M., Helander, P., Puranen, T., Salmi, A., Hægström, E., and Muinonen, K. (2018). Non-destructive controlled single-particle light scattering measurement. *Journal of Quantitative Spectroscopy and Radiative Transfer*, 204:159–164.
- Martikainen, J., Penttilä, A., Gritsevich, M., Lindqvist, H., and Muinonen, K. (2018). Spectral modeling of meteorites at uv-vis-nir wavelengths. *Journal of Quantitative Spectroscopy and Radiative Transfer*, 204:144–151.
- Mayinger, F. and Feldmann, O. (2001). *Optical Measurements: Techniques and Applications*.
- Molesini, G. (2005). Geometrical optics. In Bassani, F., Liedl, G. L., and Wyder, P., editors, *Encyclopedia of Condensed Matter Physics*, pages 257–267. Elsevier, Oxford.

- Muinonen, K., Nousiainen, T., Fast, P., Lumme, K., and Peltoniemi, J. (1996). Light scattering by gaussian random particles: Ray optics approximation. *Journal of Quantitative Spectroscopy and Radiative Transfer*, 55(5):577–601. Light Scattering by Non-Spherical Particles.
- Muinonen, K., Nousiainen, T., Lindqvist, H., Muñoz, O., and Videen, G. (2009). Light scattering by gaussian particles with internal inclusions and roughened surfaces using ray optics. *Journal of Quantitative Spectroscopy and Radiative Transfer*, 110(14):1628–1639. XI Conference on Electromagnetic and Light Scattering by Non-Spherical Particles: 2008.
- Muinonen, K., Väisänen, T., Martikainen, J., Markkanen, J., Penttilä, A., Gritsevich, M., Peltoniemi, J., Blum, J., Herranen, J., Videen, G., Maconi, G., Helander, P., Salmi, A., Kassamakov, I., and Haeggström, E. (2019). Scattering and absorption of light in planetary regoliths. *JoVE*, (149):e59607.
- Muñoz, O., Moreno, F., Guirado, D., Ramos, J., López, A., Girela, F., Jerónimo, J., Costillo, L., and Bustamante, I. (2010). Experimental determination of scattering matrices of dust particles at visible wavelengths: The iaa light scattering apparatus. *Journal of Quantitative Spectroscopy and Radiative Transfer*, 111(1):187–196.
- Onofri, F. R. A., Ren, K. F., Sentis, M., Gaubert, Q., and Pelcé, C. (2015). Experimental validation of the vectorial complex ray model on the inter-caustics scattering of oblate droplets. *Opt. Express*, 23(12):15768–15773.
- Penttilä, A., Maconi, G., Kassamakov, I., Gritsevich, M., Helander, P., Puranen, T., Hæggström, E., and Muinonen, K. (2017). Experimental light scattering by small particles: first results with a novel Mueller matrix scatterometer. In Bodermann, B., Frenner, K., and Silver, R. M., editors, *Modeling Aspects in Optical Metrology VI*, volume 10330, page 103300A. International Society for Optics and Photonics, SPIE.
- Penttilä, A., Martikainen, J., and Muinonen, K. (2022). Modeling the effect of particle size distribution on spectra for optically large particles. In *European Planetary Science Congress*, pages EPSC2022–415.
- Persson, M. V. (2013). Polarization of light by scattering of dust particles.
- Schott Advanced Optics (2023). Optics N-BK7 517642.251. <https://www.schott.com/shop/advanced-optics/en/optical-glass/n-bk7/c/glass-n-bk7>.

- Väisänen, T. (2020). *Light scattering in dense particulate media*. PhD thesis, University of Helsinki, Finland.
- Volten, H., Muñoz, O., Rol, E., de Haan, J. F., Vassen, W., Hovenier, J. W., Muinonen, K., and Nousiainen, T. (2001). Scattering matrices of mineral aerosol particles at 441.6 nm and 632.8 nm. *Journal of Geophysical Research: Atmospheres*, 106(D15):17375–17401.
- Väisänen, T., Martikainen, J., and Muinonen, K. (2020). Scattering of light by dense particulate media in the geometric optics regime. *Journal of Quantitative Spectroscopy and Radiative Transfer*, 241:106719.
- Winston, R. (2005). *Nonimaging optics*. Elsevier Academic Press, Burlington, MA.